Journal Pre-proof

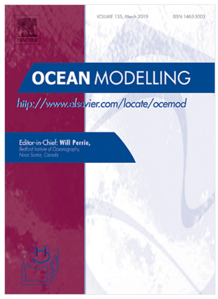

Effects of sea ice form drag on the polar oceans in the NEMO-LIM3 global ocean–sea ice model

Jean Sterlin, Michel Tsamados, Thierry Fichefet, François Massonnet, Gaia Barbic

PII: S1463-5003(23)00068-9
DOI: https://doi.org/10.1016/j.ocemod.2023.102227
Reference: OCEMOD 102227

To appear in: *Ocean Modelling*

Received date : 26 May 2022
Revised date : 14 March 2023
Accepted date : 18 May 2023

Please cite this article as: J. Sterlin, M. Tsamados, T. Fichefet et al., Effects of sea ice form drag on the polar oceans in the NEMO-LIM3 global ocean–sea ice model. *Ocean Modelling* (2023), doi: https://doi.org/10.1016/j.ocemod.2023.102227.

Highlights

Effects of sea ice form drag on the polar oceans in the NEMO-LIM3 global ocean–sea ice model

Jean Sterlin, Michel Tsamados, Thierry Fichefet, François Massonnet, Gaia Barbic

- Form drag controls the seasonality and trends in ocean surface stress under sea ice
- The mixed layer is deepened by 22–38 % in summer with form drag
- Form drag increases the summer sea surface salinity by 0.52–0.89 g/kg under sea-ice
- Arctic MIZ warms (1.0°C) and Antarctic MIZ cools (-0.5°C) in summer with form drag

Effects of sea ice form drag on the polar oceans in the NEMO-LIM3 global ocean–sea ice model

Jean Sterlin[a], Michel Tsamados[b], Thierry Fichefet[a], François Massonnet[a], Gaia Barbic[b]

[a] *Georges Lemaître Centre for Earth and Climate Research, Earth and Life Institute, Université catholique de Louvain, Louvain-la-Neuve, Belgium*
[b] *Centre for Polar Observation and Modelling, Earth Sciences, University College London, London, UK*

Abstract

The surface roughness of sea ice is highly variable because of the diversity of discrete obstacles to the flow present on the sea ice surface. These obstacles result in form drag, an effect poorly accounted for in the calculation of surface fluxes over sea ice in climate models. In this study, we implement in the ocean–sea ice model NEMO-LIM3 a variable formulation of the atmospheric and oceanic neutral drag coefficients over sea ice that includes the form drag effect. We examine the impact of this formulation on the ice cover and ocean surface properties over the past decades in the Arctic and Antarctic. Including form drag in the simulations leads to 10–50 cm thinner sea ice in the peripheral Arctic seas and ∼10 cm thicker sea ice in the Antarctic ice pack on annual means. Form drag significantly impacts summer sea surface temperatures in the marginal ice zone (+0.5 to +1.5 °C in the Arctic and −0.5 °C in the Antarctic) and sea surface salinities under the ice cover (+0.52 to +0.89 g/kg in both polar regions). The seasonality of the ocean surface stress under sea ice is reversed, with a maximum (minimum) ocean

Email address: `jean.sterlin@uclouvain.be` (Jean Sterlin)

surface stress under sea ice in summer (winter) when including form drag. However, this seasonal reversal is likely too intense in our simulations due to the underestimation of the prescribed mean floe lengths in summer. In the Arctic, the long-term declines in sea ice volume and multi-year ice are associated with decreasing neutral drag coefficients and negative trends in ocean surface stress. In the Antarctic, the trends in the neutral drag coefficients control the increase (decrease) in ocean surface stress in the Weddell and Ross (Bellingshausen and Amundsen) Seas. Form drag results in a 22–38 % deeper summer mixed layer under polar sea ice and a year-long 10–25 m deeper mixed layer in the Central Arctic. All these impacts on the ocean surface properties demonstrate the relevance of form drag for polar ocean modelling.

Keywords: sea ice model, ocean general circulation model, Arctic climate, Antarctic climate, variable neutral drag coefficients, atmosphere–sea ice–ocean interactions

---

1. Introduction

Since the late seventies, Arctic sea ice has become thinner (Kwok, 2018), younger (Maslanik et al., 2011) and smaller in extent (Serreze and Meier, 2018). The mean Arctic sea ice drift speed has substantially increased over the past decades (Rampal et al., 2009; Tandon et al., 2018; Lipatov et al., 2021) due to the decline in sea ice concentration and thickness (Olason and Notz, 2014; Tandon et al., 2018). These changes in the Arctic sea ice cover have occurred in all seasons (Stroeve and Notz, 2018). On the other hand, Antarctic sea ice has been unexpectedly expanding (Comiso et al., 2017) until recently, with a reversal in 2014 (Parkinson, 2019) followed by an absolute record low sea ice extent minimum in February 2022. Understanding these contrasting trends and regional aspects remains an open question in both model (Rackow et al., 2022) and observational studies (Fogt et al., 2022). Reconstructed and modelled Antarctic sea ice states show a significant thickening of the sea ice cover in the Weddell and Ross Seas but a thinning in the Bellingshausen and Amundsen (BA) Seas (Massonnet et al., 2013; Holland et al., 2014). Changes in local winds explain most of the observed long-term trends in sea ice drift around Antarctica (Kwok et al., 2017).

Sea ice plays a critical role in redistributing heat, momentum and freshwater between the atmosphere and the ocean at high latitudes. Surface flux anomalies in those regions impact the large-scale oceanic and atmospheric circulations and thus can affect the global climate. The turbulent fluxes of heat and momentum over sea ice are highly dependent on the top and bottom ice surface roughnesses. These two roughnesses exert a drag on the mean air and seawater flows, respectively. In turn, drag generates perturbation in the mean flow in the vicinity of the surface. These perturbations influence the mixing of scalar properties such as horizontal flow speed, temperature or humidity. Consequently, the knowledge of the drag over sea ice helps our understanding of the effects of atmosphere-ocean-ice interactions in polar regions.

Arya (1973) introduced the concept of drag partitioning over sea ice to account for the effects of small-scale roughness (skin drag) and discrete obstacles to the flow of air (form drag). Since then, the modelling community has benefited from numerous developments relating the atmospheric drag coefficients to the morphology of the ice surface (Arya, 1975; Hanssen-Bauer and Gjessing, 1988; Garbrecht et al., 2002; Birnbaum and Lüpkes, 2002; Lüpkes and Birnbaum, 2005; Lüpkes et al., 2012). Lüpkes et al. (2012) provided a hierarchy of formulas parameterizing the atmospheric neutral drag coefficients over sea ice based on physical concepts.

The drag partitioning method of Arya (1973) has been successfully adapted to ocean drag coefficient parameterizations (Lu et al., 2011). This method has paved the way for comprehensive frameworks that provide the atmospheric and oceanic neutral drag coefficients over sea ice as a function of sea ice properties. The scheme of Steiner (2001) calculates the drag coefficients over sea ice from the deformation energy and the sea ice concentration. Tsamados et al. (2014) proposed a parameterization based on an idealized floe schematic that connects the drag coefficients to ice surface features. This latter scheme includes the effect of floe edges, surface ridges or ice sails and keels, melt pond edges and skin drag.

Including form drag in sea ice models leads to significant spatial and temporal differences in the simulated Arctic sea ice thickness and drift (Tsamados et al., 2014; Martin et al., 2016; Castellani et al., 2018; Chikhar et al., 2019; Ponsoni et al., 2021). As shown by Martin et al. (2016), form drag results in a negative trend in the annual mean ocean surface stress under the Arctic sea ice cover over the period 1980-2013. This trend contrasts with the moderate increase of this diagnostic when using constant drag coefficients (Martin et al., 2014, 2016). The conclusions of Martin et al. (2016) need to be confirmed with an interactive ocean and sea-ice model setup, as these authors relied on a climatological dataset to prescribe ocean surface currents. Additionally, form drag can alter the characteristics of the mixed layer in the Arctic (Tsamados et al., 2015). Castellani et al. (2018) noted a net increase in the summer mean sea surface salinity and mixed layer depth in the Arctic when using the form drag scheme of Steiner (2001) with the Massachusetts Institute of Technology general circulation model (MITgcm). Numerical experiments carried out with the Hadley Centre Global Environment Model version 3 (HadGEM3) support evidence of an impact of form drag on the large-scale atmospheric and oceanic circulations in the Arctic (Ponsoni et al., 2021).

The main objective of this paper is to examine the sensitivity of the sea ice state and the ocean surface properties to the form drag over sea ice in the Antarctic and Arctic polar regions. The intents are two-fold: 1) revisiting past model studies incorporating a form drag formulation for the Arctic sea ice (Tsamados et al., 2014; Martin et al., 2016; Castellani et al., 2018; Chikhar et al., 2019) and 2) taking advantage of our developments to investigate the effects of the form drag in the Antarctic. For the first time, we address the analysis of the effects of form drag over sea ice in both polar regions. Our model study benefits from our global and fully coupled ocean–sea ice model setup, a refined vertical grid for the ocean model, and an extended period of 40 years for the analysis. These allow us to investigate the importance of form drag for polar sea ice and the ocean surface properties in sea ice covered regions.

We describe the methodology of this study in Section 2. We validate the modelled sea ice and investigate its sensitivity to the form drag in Section 3.1. In Section 3.2, we discuss the representation of the form drag in the model.

Next, we examine the effects of form drag on the ocean surface properties under polar sea ice in Section 3.3. Lastly, we summarize our remarks and conclude in Section 4.

2. Methods and data

2.1. The modelling framework NEMO-LIM3 and form drag over sea ice

In this study, we make use of the modelling framework Nucleus for European Modelling of the Ocean (NEMO) version 3.6 stable (SVN revision 7169) to couple the Océan PArallélisé (OPA) ocean model with the Louvain-la-Neuve sea ice model version 3 (LIM3). OPA is a finite-difference, hydrostatic, primitive equation model (Madec et al., 2017) using the Boussinesq approximation. LIM3 is a state-of-the-art thermodynamic-dynamic sea ice model (Vancoppenolle et al., 2009; Rousset et al., 2015). LIM3 features, notably, a discrete subgrid-scale ice thickness distribution (ITD) (Thorndike et al., 1975), an elastic-viscous-plastic (EVP) rheology formulation (Hunke and Dukowicz, 1997), and an energy-conserving thermodynamic model (Bitz and Lipscomb, 1999).

Our version of LIM3 includes a lateral ice melt scheme based on the prescription of the mean floe length L_f of Lüpkes et al. (2012):

$$L_f(A) = L_{min}\left(\frac{A_*}{A_* - A}\right)^{\beta} \tag{1}$$

where L_{min} and L_{max} are constant parameters related to the minimum (8 m) and maximum (300 m) floe lengths, respectively. A is the ice concentration. The parameter A_* prevents a singularity when the ice concentration tends to zero: $A_* = 1/[1-(L_{min}/L_{max})^{1/\beta}]$. Equation 1 also prescribes the mean floe length in the form drag formalism of Tsamados et al. (2014). According to Lüpkes et al. (2012), $\beta = 0.3$ is more representative of sea ice conditions in the Antarctic and Western Fram Strait, whereas $\beta = 1.4$ better reflects sea ice conditions in Eastern Fram Strait. These different values for β highlight the limit of such formulation, as Equation 1 cannot express the full range of variability of the observed floe lengths. We use this formulation as a first order method to represent the change in floe length across the marginal ice zone as a function of sea ice concentration. We set the coefficient β equal to 0.5 as in the study of Tsamados et al. (2014).

The atmospheric forcing follows the protocol of the second experiment from the Coordinated Ocean-ice Reference Experiments (CORE-II) (Griffies et al., 2009), as implemented in NEMO-LIM3 (Madec et al., 2017). Bulk formulas define the wind stress ($\vec{\tau}_{ax}$), the latent ($Q_{E,ax}$) and sensible ($Q_{H,ax}$) turbulent heat fluxes across the atmosphere (subscript a) and ocean ($x = o$) or sea ice ($x = i$) interfaces (Large and Yeager, 2004, 2008):

$$\vec{\tau}_{ax} = \rho_a C_{D,ax}\, \vec{u}_a\, |\vec{u}_a| \tag{2}$$

$$Q_{E,ax} = \rho_a C_{E,ax} L_v\ (q_a(z) - q_x)\ |\vec{u}_a| \tag{3}$$

$$Q_{H,ax} = \rho_a C_{H,ax} c_p\ (\theta_a(z) - \theta_x)\ |\vec{u}_a| \tag{4}$$

where $\rho_a = 1.22\,\mathrm{kg/m^3}$ is the air density, $L_v = 2.5 \times 10^6\,\mathrm{J/kg}$ is the latent heat of vaporization, $c_p = 1000.5\,\mathrm{J/kg/K}$ is the specific heat of the air, $\vec{u}_a(z)$ is the wind velocity at height $z = 10\,\mathrm{m}$, $q_a(z)$ is the air specific humidity and $\theta_a(z)$ the air temperature at height $z = 2\,\mathrm{m}$, q_x is the specific humidity and θ_x the temperature at the surface (ocean or sea ice). The transfer coefficients for momentum ($C_{D,ax}$), latent ($C_{E,ax}$) and sensible heat fluxes ($C_{H,ax}$) are specific to the surface type (ocean or sea ice). Note that these formulations exclude the effect of a turning angle on the surface fluxes of heat and momentum. Additionally, the wind velocity is assumed to exceed ocean surface currents ($|\vec{u}_a| \gg |\vec{u}_o|$) and sea ice drift ($|\vec{u}_a| \gg |\vec{u}_i|$).

The formalism of Large and Yeager (2004, 2008) prescribes the transfer coefficients at the atmosphere–ocean interface as well as stability coefficients to account for atmospheric stratification effects over the open water fraction. In the case of sea ice, the transfer coefficients are set constant in the default configuration of NEMO-LIM3. As a second formulation, we prescribe the transfer coefficients over sea ice using the variable formulation of the atmospheric neutral drag coefficients of Tsamados et al. (2014). Contrary to this study, we do not consider stability effects in the atmospheric boundary layer over sea ice. Lastly, NEMO-LIM3 does not include stability effects in the ocean boundary layer, neither for open water nor under sea ice.

The turbulent fluxes of momentum ($\vec{\tau}_{io}$) and heat (Q_{io}) at the ice-ocean interface (subscript io) are prescribed using Equations 5 and 6, respectively:

$$\vec{\tau}_{io} = \rho_w C_w \left[\vec{u}_i - \vec{u}_o\right] |\vec{u}_i - \vec{u}_o| \tag{5}$$

$$Q_{io} = \rho_w C_w C_h u^*_{io} \left[\theta_i^{bottom} - SST\right] |\vec{u}_i - \vec{u}_o| \tag{6}$$

where ρ_w is the density of seawater, θ_i^{bottom} is the basal temperature of sea ice, C_h is a constant ocean heat transfer coefficient equal to 5.7×10^{-3} and C_w is an oceanic drag coefficient. The oceanic drag coefficient is either set constant or prescribed using the variable oceanic neutral drag coefficient formulation of Tsamados et al. (2014). The expression of Q_{io} depends on the friction velocity u^*_{io}, which uses the ice-ocean root mean square velocity difference (Vancoppenolle et al., 2009). The ocean surface stress ($\vec{\tau}_{oce}$) is computed as $\vec{\tau}_{oce} = (1 - A)\vec{\tau}_{ao} + A\vec{\tau}_{io}$ (Large and Yeager, 2008; Rousset et al., 2015). The ocean surface heat flux (including Q_{io}) is calculated using the same ice concentration averaging method.

The implementation of the variable neutral drag coefficients over sea ice of Tsamados et al. (2014) in our setup is closely related to the implementation of this formalism in the Icepack sea ice column model (Hunke et al., 2021), part of the CICE-Consortium. See the supplementary material of this manuscript for a comprehensive list of the parameters and values used in the form drag formalism. This formalism decomposes the atmospheric (ANDC) and oceanic (ONDC) neutral drag coefficients C_{da} and C_{dw} into the sum of individual form drag contributions associated with discrete obstacles to the flow of air or seawater:

$$C_{da} = C_{da}^{rdg} + C_{da}^{floe} + C_{da}^{skin} + C_{da}^{pnd} \tag{7}$$

$$C_{dw} = C_{dw}^{rdg} + C_{dw}^{floe} + C_{dw}^{skin} \tag{8}$$

The subscripts a and w are related to the air and seawater mediums, respectively. The form drag contributions include the effects of ice ridges (C_{da}^{rdg} and C_{dw}^{rdg}), floe edges (C_{da}^{floe} and C_{dw}^{floe}), surface skin (C_{da}^{skin} and C_{dw}^{skin}) and melt pond edges (C_{da}^{pnd}). Melt ponds have no impact on the oceanic neutral drag coefficients. To help the reader, Figure 1 presents a schematic showing the idealized floe of Tsamados et al. (2014), its relation with the form and skin drag coefficients as well as the turbulent fluxes of momentum, latent and sensible heat exchanged between the atmosphere, ocean, sea ice systems.

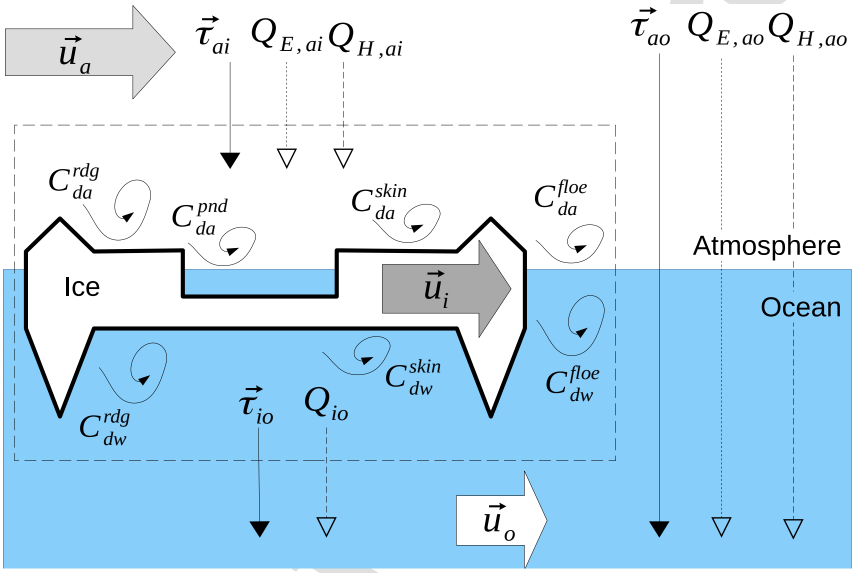

Figure 1: Schematic representation of the idealized floe of Tsamados et al. (2014) in the context of the coupling between the atmosphere, ocean, sea ice systems. The horizontal arrows containing $\vec{u}_a$, $\vec{u}_o$ and $\vec{u}_i$ indicate the mean horizontal air, ocean and sea ice velocities, respectively. Solid, dotted and dashed vertical arrows represents the turbulent fluxes of momentum ($\vec{\tau}$), latent (Q_E) and sensible heat (Q_H), respectively. The subscript i is for sea ice, a is for the air or atmosphere, o and w are for the ocean or seawater. The form drag (C_{dx}^{rdg}, C_{dx}^{floe}, C_{da}^{pnd}) and skin drag (C_{dx}^{skin}) coefficients constituting the total neutral drag coefficients are displayed near the corresponding surface feature of the idealized floe, where x equals a or w. The whirling arrows depict perturbations in the mean flow.

The transfer coefficients for momentum, latent and sensible heat fluxes at the atmosphere-ice interface in Equations 2–4 are set equal to the neutral drag coefficient C_{da}, assuming identical values for these coefficients: $C_{D,ai} = C_{E,ai} = C_{H,ai} = C_{da}$. Direct measurements of the atmospheric transfer coefficient over sea ice suggest smaller transfer coefficients for latent and sensible heat fluxes than for momentum (Schröder, 2003). We leave the question of the effect of such inequality in the transfer coefficients open for future studies. The oceanic drag coefficient at the ocean-ice interface in Equations 5 and 6 is set equal to the neutral drag coefficient: $C_w = C_{dw}$.

The general expression of the form drag coefficients derives from the Monin-Obukhov similarity theory assuming a logarithmic fluid velocity profile (Hanssen-Bauer and Gjessing, 1988). This expression is valid for both the ocean and the atmosphere, and assumes no Coriolis forces. One can define this expression assuming no Coriolis effect and for a reference level of 10 m as:

$$C_{dx}^{form} = \frac{1}{2} c S_c^2 \frac{H}{D} A \left[\frac{\ln(H/z_0)}{\ln(10/z_0)} \right]^2 \tag{9}$$

where the superscript $form$ corresponds to the form drag contribution of ridges ($form = rdg$), floes ($form = floe$) or melt ponds ($form = pnd$). The subscript x is either for the air (a) or seawater (w) mediums. c is a constant local form drag coefficient set to 0.20 in this study. More recently, Zu et al. (2021) recommended 0.57 for the local form drag coefficient of keels used in C_{dw}^{rdg}. H is the height of the obstacles (sails, keels, floe or melt pond edges) and D is the distance separating them. z_0 represents the roughness length of the upstream surface type. Moreover, Equation 9 relies on sheltering functions (S_c) expressing the flow attenuation downstream of the obstacles:

$$S_c^2 = \begin{cases} 1 - \exp\left(-0.18D/H\right) & rdg \\ 1 - \exp\left(-22\beta(1-A)\right) & floe \\ A_p^{1/(10\beta)} & pnd \end{cases} \tag{10}$$

where A_p is the melt pond concentration. We keep the sheltering function selected by Tsamados et al. (2014) for the contributions due to ridges (sails and keels). However, we select the formulation of Lüpkes et al. (2012) adopted in the Icepack model (Hunke et al., 2021) regarding the sheltering functions for floe and melt pond edges. These later two sheltering functions use the power coefficient β of the prescribed floe length equation (Equation 1) to better reflect the changes in floe length with the ice concentration. Lastly, the general expression of the surface skin drag coefficients is:

$$C_{dx}^{skin} = A\left(1 - m_x\frac{H}{D}\right)c \quad \text{if} \quad \frac{H}{D} \geq \frac{1}{m_x} \tag{11}$$

where m_x is an atmospheric ($x = a$) or oceanic ($x = o$) skin drag parameter assumed constant here and c is the unobstructed skin drag coefficient. H/D is the ratio of the ridge height (sails or keels) over the distance between ridges (sails or keels).

In our model setup, the reference depth in the expression of the ocean form drag coefficients is 10 m, even though the ocean surface currents are defined at 0.5 m depth. Roy et al. (2015) advise against such a reference depth when the vertical resolution of the ocean model near the surface is sufficiently high (∼1 m) to resolve the planetary boundary layer of the ocean. Based on this study, our simulations likely overestimate Arctic sea ice drift. Roy et al.

(2015) proposed a method to better account for the vertical ocean velocity profile near the surface in the ocean drag definition. This method may lead to numerical instabilities due to the increase in the calculated ocean drag coefficients. They reduced the time step of their ocean model to 600 s to solve this issue. We faced similar numerical instabilities when implementing form drag in NEMO-LIM3 because of the variability of the drag coefficients. We lowered the time step of the ocean (sea ice) model to 900 s (5400 s) to ensure numerical stability. Changing the reference depth from 10 m to 0.5 m in the general form drag expression (Equation 9) is equivalent to multiplying the ocean form drag contributions associated with keels and floes by a factor of two. This would further alter the stability of the model. Therefore, more work is needed to reconcile the definition of the variable drag coefficients with the reference depth of the ocean surface currents while maintaining the model stability. In the meantime, this discrepancy does not question the ability of the model to simulate the variability in the neutral drag coefficients.

2.2. Intermediate sea ice variables

To evaluate C_{da} and C_{dw}, the variables needed are the freeboard (H_f) and the draft (H_d) of the floes, the distance between floes (D_f), the melt pond size (L_p) and the elevation of the ice surface relative to the melt pond surface (H_p). Moreover, ice ridges consist of surface ridges also named sails and bottom surface ridges or keels. Thus, the evaluation of the neutral drag coefficients additionally requires the distance between sails (D_s) and keels (D_k), and the vertical height of these obstacles. The sail height (H_s) and keel depth (H_k) have for reference the ice surface and bottom surface elevation, respectively (Hunke et al., 2021). We obtain these by subtracting the freeboard (draft) height from the sail (keel) height.

H_f and H_d are calculated from the hydrostatic balance using the mean volume of snow (v_s) and ice (v_i) per grid cell. Melt ponds are supposed to be at equilibrium with the ocean surface ($H_p = H_f$), with no effect on the hydrostatic balance of the floes. This assumption is justified in the Arctic, as melt ponds are above sea level only during the first weeks of their onsets (Eicken, 2002). We keep this assumption unchanged in the Southern Hemisphere in the absence of observational evidence.

Drafts may exceed the ice thickness when the mass of snow is sufficiently large to submerge the ice surface below sea level. Flooding of the ice surface is frequent in the Antarctic, e.g., after important snowfall events on relatively thin ice. When flooding occurs, a fraction of snow is converted to ice in the hydrostatic balance so that the draft equals the ice thickness (Leppäranta, 1983).

Tsamados et al. (2014) estimate D_s, D_k, H_s and H_k by identifying the simulated deformed ice volume and concentration to the total volume and area of sails and keels per grid cell using an idealized floe schematic (see Figure 1 of Tsamados et al. (2014)). To estimate the deformed ice quantities, we have implemented tracers of level-ice volume and concentration in LIM3. These tracers represent the quantities of sea ice that have not undergone ridging or rafting events. The difference between the ice volume (concentration) and the tracer of level-ice volume (concentration) is defined to be equal to the deformed ice volume (concentration).

Following Tsamados et al. (2014), we set the ratio of the keel depth to sail height equal to 4. This ratio is within the 3.5–4.5 range for the most frequent maximum keel depth to sail height ratio (Strub-Klein and Sudom, 2012). In the Antarctic, Tin and Jeffries (2003) estimated a keel-to-sail ratio of 5.6 ± 1.8.

We set the distance between keels equal to the distance between sails based on (Tsamados et al., 2014). It excludes rubble piles and widow ridges, i.e. keels without associated sails. Rubble piles have extremely low keel depth-to-width ratios compared to other ice ridge types (Tin and Jeffries, 2003). Thus, the surface skin contribution is more appropriate for accounting for the effect of rubble piles.

We select 22° for the slope angle of sails and keels in the implementation of the form drag formalism (Tsamados et al., 2014; Martin et al., 2016; Hunke et al., 2021). Using the idealized floe schematic of Tsamados et al. (2014) and the mean width-to-height ratios from Strub-Klein and Sudom (2012), we find that keel slope angles are $\sim$22° and sail slope angles are $\sim$28° for Arctic first-year ice ridges. Tin and Jeffries (2003) estimated keel slope angles of $(15 \pm 8)^\circ$ and sail slope angles of $(10 \pm 5)^\circ$ in the Southern Ocean.

The porosity of sea ice is set to 0.30 in LIM3 based on in-situ observations (Leppäranta et al., 1995; Høyland, 2002). This value is larger than the one selected by Tsamados et al. (2014) for the form drag. However, we keep the default value from LIM3 for sea ice porosity to avoid discrepancies between the simulated deformed ice quantities and the total volume and area of sails and keels identified from the idealized floe schematic of Tsamados et al. (2014).

D_f is calculated by assuming periodically distributed square floes (Lüpkes and Birnbaum, 2005; Tsamados et al., 2014). This method requires the floe length, here prescribed by Equation 1.

Lastly, the so-called topographic scheme parameterizes melt ponds in the model (Flocco et al., 2010; Sterlin et al., 2021). The refreezing mechanism for melt ponds is given by Holland et al. (2012), using the refreezing temperature threshold of $-0.15\,^{\circ}$C instead of $-2.00\,^{\circ}$C. The melt pond scheme provides the melt pond area fraction, which is the argument of the equation for L_p (Lüpkes et al., 2012, Equation 45).

2.3. Experimental design

We perform two simulations with a global configuration of NEMO-LIM3 from 1958 to 2019. The analysis is restricted to the last 40 years of this period to exclude spin-up effects, unless otherwise stated. The first experiment (FORM) takes the variable neutral drag coefficients of Tsamados et al. (2014) to calculate the transfer coefficients over sea ice. The second experiment (SKIN) uses constant drag coefficients over sea ice. These constants are determined as the global means of the variable neutral drag coefficients simulated in the FORM run and weighted by the sea ice area over 1980–2019. The constant drag coefficients in the SKIN run are $C_{da} = 1.49 \times 10^{-3}$ and $C_{dw} = 6.71 \times 10^{-3}$. As for a comparison, the standard drag coefficients in LIM3 are 1.40×10^{-3} and 5.0×10^{-3} for C_{da} and C_{dw}, respectively. This choice of coefficients for the SKIN run allows investigating the effect of form drag rather than the differences between the FORM run and the standard configuration of LIM3.

The ocean and ice models share the same 1° curvilinear tripolar horizontal ORCA grid from Madec and Imbard (1996). This horizontal grid has a cell edge length of ∼112 km at the equator, down to ∼46 km in the Arctic Ocean.

The vertical grid includes 75 levels in partial step z-coordinates. The vertical resolution of this grid decreases from 1 m at the ocean surface down to 200 m near the ocean floor, following a double hyperbolic tangent function.

We select the Japanese 55-year reanalysis (JRA-55) (Kobayashi et al., 2015) to provide the atmospheric surface variables required by CORE-II. JRA-55 is a sub-daily (3 h) high-resolution (∼55 km) atmospheric reanalysis based on a 4D-var data assimilation scheme performed by the Japan Meteorological Agency. This reanalysis produced reasonable representations of sea ice in polar regions using the same model configuration as ours (Barthélemy et al., 2017; Sterlin et al., 2021). The reader is redirected to the study of Sterlin et al. (2021) for a complete description of the present model configuration.

2.4. Observations

We evaluate the simulated sea ice concentrations in the FORM and SKIN runs against the Sea Ice Concentrations from Nimbus-7 SMMR and DMSP SSM/I-SSMIS Passive Microwave Data product (Cavalieri et al., 1996). The National Snow and Ice Data Center (NSIDC) references this dataset as the NSIDC-0051 product. This dataset is constructed using the NASA Team Algorithm.

We assess the representation of the sea ice drift in NEMO-LIM3 with version 4.1 of the Polar Pathfinder Daily 25 km EASE-Grid Sea Ice Motion Vectors product (Tschudi et al., 2019), hereafter referred to as the NSIDC-0116 product. One may attempt to correct the meridional drift bias in the NSIDC-0116 product by multiplying the ice velocities by a factor of 1.4 (Haumann et al., 2016). However, the NSIDC-0116 product remains subject to uncertainties that a constant factor cannot alone solve, particularly during summer (Sumata et al., 2015). Further, the errors in this product are greater when 1) the ice concentrations are lower, 2) the ice thicknesses are smaller, 3) the ice speeds are higher (Sumata et al., 2014). This strongly suggests regional differences in the uncertainties of the NSIDC-0116 product. The qualities of the NSIDC-0116 product are the long-term daily frequency ice drift vector components interpolated on an Eulerian grid.

The simulated effective sea ice thicknesses or ice thicknesses and the total sea ice volumes from NEMO-LIM3 are evaluated against the Pan-Arctic Ice Ocean Modeling and Assimilation System (PIOMAS) and Global Ice-Ocean Modeling and Assimilation System (GIOMAS) products (Zhang, 2014). PIOMAS and GIOMAS are not pure observational products but reanalyses of the ocean and ice systems. The former assimilates observed sea ice concentrations and sea surface temperatures in the Arctic, whereas the latter is a global model assimilating only observed sea ice concentrations. Uncertainties in the PIOMAS dataset are relatively well studied (Schweiger et al., 2011). GIOMAS likely inherits from some of PIOMAS's biases as the two share the same assimilation system (Shi et al., 2021; Liao et al., 2022). The knowledge of these uncertainties and the consistent approach to reconstructing the sea ice thickness over the past decades are valuable assets for our analysis.

3. Result and discussion

3.1. Sea ice state

3.1.1. Sea ice concentration and total sea ice area

The mean seasonal cycle of the Arctic sea ice area (SIA) is relatively well represented in the FORM and SKIN runs compared to the NSIDC-0051 product (Cavalieri et al., 1996), as shown in Figure 2a, but with some differences detailed below. NEMO-LIM3 underestimates (overestimates) the Arctic SIA in summer (winter) by 15 to 27 % (∼12 %) compared to the NSIDC-0051 product. Further, the seasonal minimum in Arctic SIA is simulated two to three weeks in advance of the NSIDC-0051 observations. These issues are common to other model studies conducted with NEMO-LIM3 and using a similar model setup to ours (e.g., Vancoppenolle et al., 2009; Docquier et al., 2017; Massonnet et al., 2019). On the other hand, NEMO-LIM3 simulates the position of the ice edge (here defined as the 15 % ice concentration line) reasonably well in the Arctic (Figure 3c). Uncertainties in the atmospheric forcing likely explain minor spatial differences between the simulated and observed sea ice concentrations in the Arctic (Sterlin et al., 2021).

In the Antarctic, the timing of the mean seasonal cycles of the simulated SIA is in phase with the observed one from the NSIDC-0051 product (Figure 2b). NEMO-LIM3 simulates the spatial distribution of the sea ice concentration in the Antarctic relatively well (Figure 3b). The two model runs overestimate the sea ice concentration in most of the Antarctic ice pack (Figure 3c). This bias was reported for simulations using various atmospheric forcings (Barthélemy et al., 2017) and previous model versions of NEMO-LIM3 (Vancoppenolle et al., 2009; Massonnet et al., 2019). Lastly,

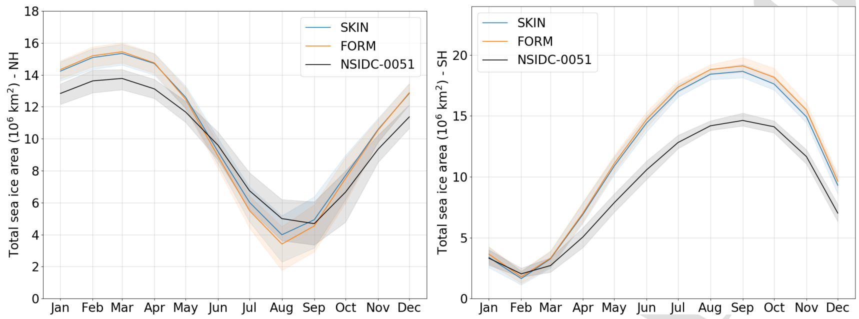

(a) (b)

Figure 2: Mean seasonal cycles of the total sea ice area (10^6 km^2) in the Northern (2a) and Southern (2b) Hemispheres over 1980–2019 from the SKIN run (blue), FORM run (orange) and the NSIDC-0051 product (black). Shaded areas are enclosed by the lowest 10^{th} and highest 90^{th} percentiles of the total sea ice area from the SKIN run (blue), FORM run (orange) and NSIDC-0551 product (black).

our model configuration does not allow the resolution of the extrema in sea ice concentration along the coastline of Antarctica. The poor representation of katabatic winds in the atmospheric forcing (Kobayashi et al., 2015), the coarse model resolution in coastal regions and the lack of land-fast ice and coastal polynyas in the simulations (Nihashi and Ohshima, 2015) prevent the representation of such extrema in sea ice concentration.

Table 1 presents the interdecadal trends in SIA in the Arctic and Antarctic and specific regions of the Southern Ocean. The Indian sector is enclosed by the longitudes 20 °E and 90 °E, and the Pacific sector by the longitudes 90 °E and 150 °E. The annual mean Arctic SIA calculated from the NSIDC-0051 product steadily declined over 1980–2019 at the rate of $0.59 \times 10^6\,\mathrm{km}^2$ per decade. Both runs capture the observed decline in Arctic SIA and its

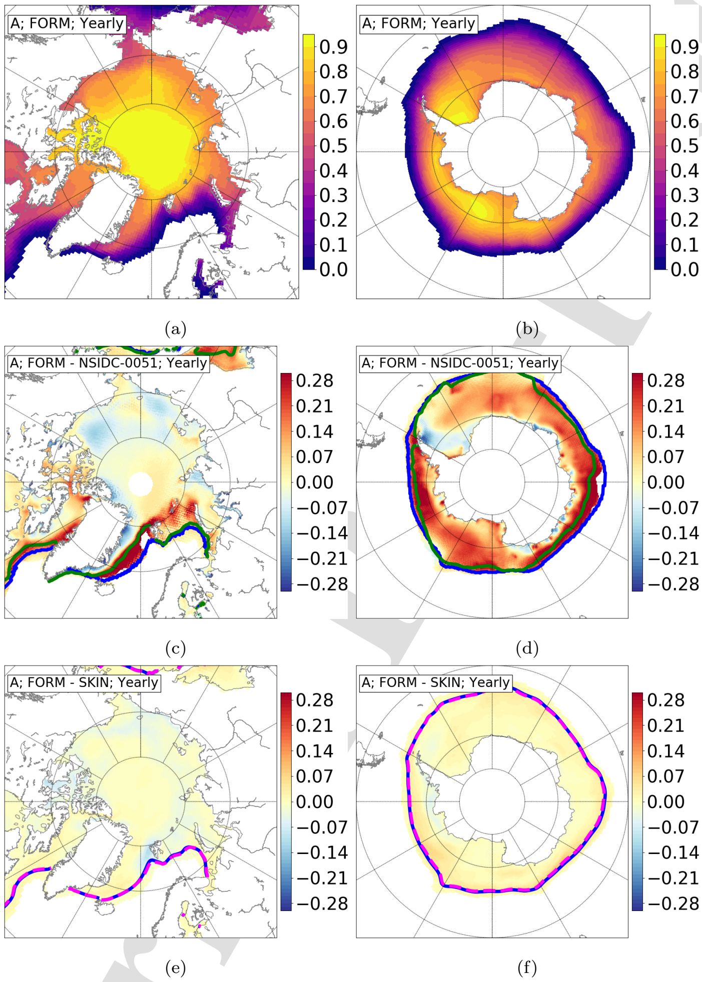

Figure 3: Annual mean sea ice concentrations from the FORM run (3a, 3b) and differences in annual mean sea ice concentration from the FORM run and the NSIDC-0051 product (3c, 3d) and between the FORM and SKIN runs (3e, 3f) in the Northern (3a-3e) and Southern (3b-3f) Hemispheres over 1980–2019. The 15 % sea ice concentration contours from the NSIDC-0051 product and the FORM run are shown in green and blue, respectively. The dashed magenta line indicates the 15 % sea ice concentration contour from the SKIN run.

statistical significance correctly. On the contrary, the interdecadal trends in the observed Antarctic sea ice extent are regional and weakly positive (Turner et al., 2015; Comiso et al., 2017). The observed sea ice extent increased in the Ross and Weddell Seas but decreased in the Bellingshausen and Amundsen (BA) Seas over the past decades. NEMO-LIM3 reproduces the main characteristics of the regional and pan-Antarctic long-term trends in SIA. The simulated trends in SIA in the Ross Sea are significantly positive and approximately three times greater than the equivalent trend from the NSIDC-0051 product. The associated changes in the simulated sea ice concentration impact principally the marginal ice zone (MIZ) of the Antarctic ice pack (not shown) where passive microwave remote sensing is prone to errors (Cavalieri et al., 1996).

Table 1: Trends in the annual mean total sea ice area (10^6 km^2 per decade) over 1980–2019 from the FORM and SKIN runs, and the NSIDC-0051 observational product. The trends are calculated in the Northern (NH) and Southern (SH) Hemispheres and specific regions of the Antarctic: the Weddell Sea (60 °W to 20 °E), the Bellingshausen and Amundsen (BA) Seas (60 °W to 130 °W), the Ross Sea (130 °W to 160 °E), the Pacific (90 °E to 150 °E) and Indian (20 °E to 90 °E) sectors of the Antarctic. Values in bold indicate a p-value less than 0.01.

	NH	SH	Weddell	BA Seas	Ross	Pacific	Indian
FORM	**-0.57**	0.26	0.08	0.01	**0.13**	0.02	0.02
SKIN	**-0.60**	0.26	0.09	0.01	**0.13**	0.02	0.01
NSIDC-0051	**-0.59**	0.16	0.06	-0.01	0.05	0.03	0.03

The formulation of the neutral drag coefficients in NEMO-LIM3 leads to only minor differences in terms of the simulated SIA and sea ice concentration. The mean seasonal cycles of the Arctic SIA in the FORM and SKIN runs differ in summer by a few $0.54 \times 10^6\,\mathrm{km}^2$ (Figure 2a). The spatial distribution of the annual mean Arctic sea ice concentration exhibits few differences between the two runs (Figure 3e). In the Antarctic, during wintertime, the SIA from the FORM run is slightly larger than the one from the SKIN run (Figure 2b). The sea ice concentration in the Antarctic MIZ is moderately higher when including form drag (Figure 3f). Lastly, the trends in SIA are nearly identical in the two simulations (Table 1).

3.1.2. Sea ice thickness and total sea ice volume

The mean seasonal cycles in the Arctic of the total sea ice volume (SIV) reconstructed by PIOMAS and GIOMAS and simulated by NEMO-LIM3 are comparable in summer and autumn (Figure 4a). The differences are significant only in winter and spring. In October, the differences in Arctic SIV from NEMO-LIM3 and PIOMAS are less than the uncertainty of $1.35 \times 10^3\,\mathrm{km}^3$ given for the PIOMAS product (Schweiger et al., 2011). The March SIV from the FORM run is $2.7 \times 10^3\,\mathrm{km}^3$ greater than the SIV from PIOMAS. This difference slightly exceeds the PIOMAS uncertainty of $2.25 \times 10^3\,\mathrm{km}^3$ (Schweiger et al., 2011). GIOMAS is less constrained by observations than PIOMAS. As such, Figure 4a gives the seasonal climatology of the Arctic SIV from the GIOMAS dataset only as an indication.

In the Southern Ocean, the simulated SIV replicates the climatology from the GIOMAS dataset (Figure 4b) with two noticeable differences. The NEMO-LIM3 seasonal minimum in SIV is approximately 60 % times larger than in GIOMAS. The simulated winter maxima are lagged by one month compared to GIOMAS. PIOMAS and GIOMAS are not pure observations

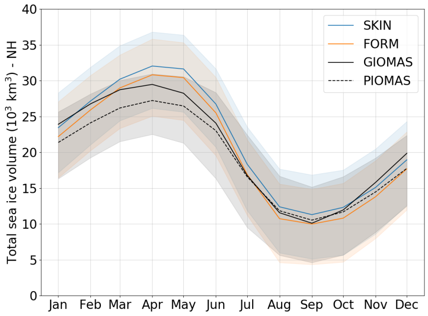

(a)

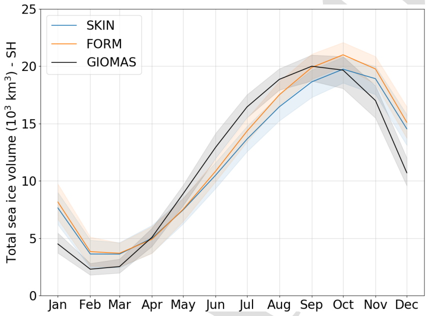

(b)

Figure 4: Same as in Figure 2 but for the total sea ice volume in the Northern (4a) and Southern (4b) Hemispheres. The dashed (continuous) black line corresponds to the PIOMAS (GIOMAS) dataset. Note that, for clarity, the shaded area enclosed by the 10^{th} and 90^{th} percentiles of the total sea ice volume from the GIOMAS dataset is omitted in Figure 4a.

as these products rely on models with similar physics to NEMO-LIM3 to reconstruct the sea ice state. The simulated seasonal cycles of the SIV from our two runs are consistent with Barthélemy et al. (2017). The latter authors selected the JRA-55 atmospheric reanalysis to force NEMO-LIM3 as in the present study. Additionally, the differences between GIOMAS and NEMO-LIM3 are similar to the past results from Massonnet et al. (2019).

The spatial distribution of the simulated Arctic sea ice thickness (sea ice volumes per grid cell area) is relatively realistic (Figure 5a) and compares well with the principal Arctic sea ice thickness observational products (Wang et al., 2016). However, the comparison of FORM with the PIOMAS dataset reveals a difference in the gradient of sea ice thickness in the region of Fram Strait (Figure 5c). Sensitivity studies conducted with NEMO-LIM3 strongly

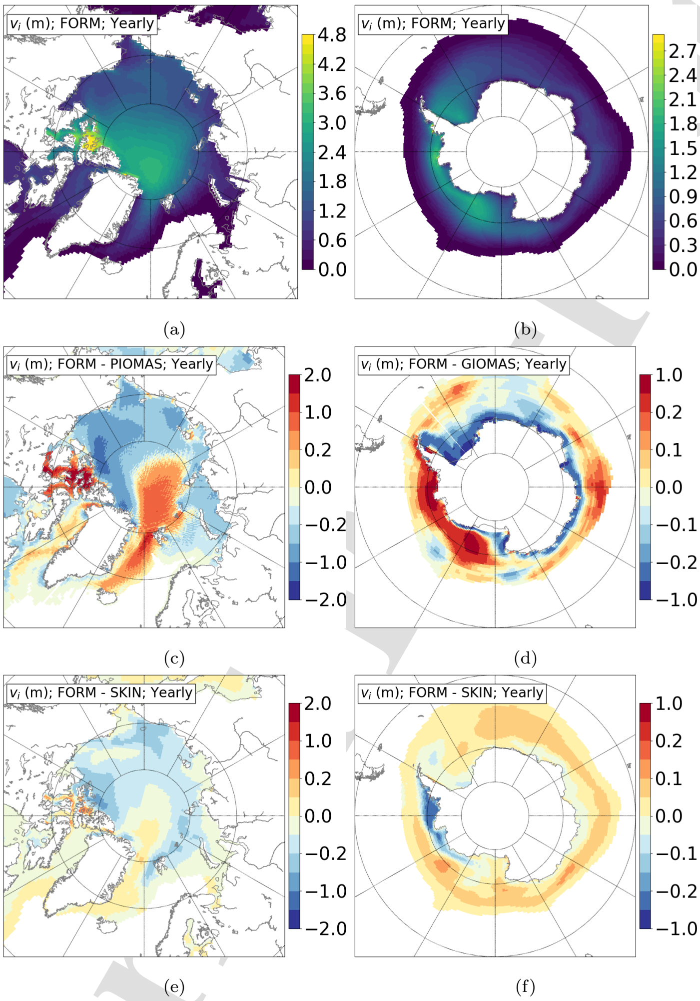

Figure 5: Annual mean sea ice thicknesses (sea ice volumes per grid cell area, in m^3/m^2), from the FORM run (5a, 5b). Differences in the annual mean sea ice thickness from the FORM run and the PIOMAS dataset in the Arctic (5c) and from the FORM run and the GIOMAS dataset in the Antarctic (5d). Differences in the annual mean sea ice thickness from the FORM and SKIN runs (5e, 5f). Annual means are calculated over 1980–2019 in the Northern (5a-5e) and Southern (5b-5f) Hemispheres.

point to the uncertainties in the atmospheric forcing for explaining this difference (Sterlin et al., 2021). On the other hand, observational products show that the reconstructed sea ice from PIOMAS is too thin in the Beaufort Sea area and too thick north of Greenland and the Canadian Arctic Archipelago (CAA) (Wang et al., 2016). These biases in PIOMAS indicate a better agreement of the FORM run with observations in these regions than one may infer from Figures 5a and 5c.

ICESat observations between 2003 and 2008 in the Southern Hemisphere show that sea ice is the thickest in the western regions of the Southern Ocean and along the coastline of Antarctica (Kurtz and Markus, 2012). NEMO-LIM3 simulates realistic thick sea ice up to 2 m in the Western Antarctic (Figure 5b). The modelled sea ice is too thin along the coast of Antarctica because of the coarse grid resolution, the poor representation of katabatic winds and land-fast ice. GIOMAS underestimates the ice thickness close to the shore of Antarctica but overestimates this quantity away from the shore in the marginal seas (Liao et al., 2022). Shi et al. (2021) confirmed this issue in the Weddell Sea. These issues explain most of the spatial differences in sea ice thickness between the FORM run and the GIOMAS product around Antarctica (Figure 5d).

The impacts of the neutral drag coefficient formulation on the SIV and the mean ice thickness vary between the Northern and Southern Hemispheres. In the Northern Hemisphere, the SIV simulated in the FORM run is $\sim$1300 km^3 smaller than in the SKIN run all year round (Figure 4a). This difference between the two runs is due to the mean ice thickness in the FORM run being smaller than in the reference SKIN run by about 0.1–0.5 m in most of the peripheral seas of the Central Arctic (Figure 5e). As a result, including form drag slightly exacerbates the negative difference in mean ice thickness between the SKIN run and PIOMAS in the same regions (Figure 5c). On the other hand, the spatial pattern of the differences in Arctic sea ice thickness between NEMO-LIM3 and PIOMAS is unchanged by the inclusion of form drag. As in the study of Tsamados et al. (2014), thermodynamical processes rather than sea ice dynamics control the differences in mean ice thickness between our two model runs (not shown).

In the Southern Hemisphere, the mean SIV is in winter $\sim$1300 km^3 higher in the FORM run than in the SKIN run (Figure 4b) because of thicker sea ice in the MIZ and a more consolidated ice pack (Figure 5f). These differences in ice thickness between the two runs are less significant in summer and early winter (not shown). Additionally, the sea ice thickness in the BA Seas (between 60 °W to 120 °W) from the FORM run is smaller than in the SKIN run all year-round (Figure 5f).

Evidence from submarine sonars and satellite altimeters shows a thinning of the sea ice cover and a decline in the Arctic SIV since 1958 (Kwok, 2018). The trend in the annual mean SIV from the PIOMAS dataset is -3.13×10^3 km^3 over 1980–2019 (Table 2), with an estimated uncertainty of 1×10^3 km^3 per decade (Schweiger et al., 2011). The simulated trends in annual mean Arctic SIV from the SKIN and FORM runs are close and within the uncertainty range of this trend from the PIOMAS dataset (Table 2). The decline in Arctic SIV from ICESat and CryoSat-2 satellite observations (2003–2018) is -2.87×10^3 and -5.13×10^3 km^3 per decade in winter and fall, respectively (Kwok, 2018). Neither PIOMAS nor NEMO-LIM3 reproduces the observed trend in fall from the ICESat and CryoSat-2 satellite observations. The lifespan of these satellite platforms is relatively short (15 years in total) compared to the four-decade long trends presented in Table 2. The 2007 record minimum in sea ice extent and the associated loss in the MYI area heavily influence the time series of ICESat (Kwok, 2018).

Table 2: Trends in the annual mean total sea ice volume (10^3 km^3 per decade) over 1980–2019 from the FORM and SKIN runs, and the PIOMAS and GIOMAS datasets. The trends are calculated in the Northern (NH) and Southern (SH) Hemispheres and specific regions of the Southern Ocean: the Weddell Sea, the Bellingshausen and Amundsen (BA) Seas, the Ross Sea and the Pacific and Indian sectors of the Southern Ocean. The regions are defined in Table 1. Values in bold indicate a p-value less than 0.01.

	NH	SH	Weddell	BA Seas	Ross	Pacific	Indian
FORM	**-3.47**	0.29	0.20	**-0.18**	**0.24**	0.02	0.02
SKIN	**-3.58**	0.28	**0.21**	**-0.20**	**0.26**	0.02	-0.00
PIOMAS	**-3.13**	-	-	-	-	-	-
GIOMAS	**-2.58**	0.55	**0.38**	0.02	0.05	0.05	0.05

The long-term trend in the annual mean SIV from the GIOMAS dataset is positive in the Southern Hemisphere but not statistically significant (Table 2). In addition to the GIOMAS product, Massonnet et al. (2013) performed a similar model reconstruction of the Antarctic sea ice thickness using an ensemble Kalman filter to assimilate the ice concentration. Although these authors showed a positive trend in the pan-Antarctic SIV over the past decades, they pointed to high temporal variability in the time series of SIV and regional dissimilarities in the calculated trends in SIV. We find a good correspondence between the regional trends in the Antarctic SIV from the

FORM and SKIN runs, their statistical significance and those of Massonnet et al. (2013). These are gains in the annual mean SIV in the Weddell and Ross Seas but a decline in the SIV in the BA Seas (Table 2). While there is good agreement in the Weddell Sea on the sign of the trends in SIV across most modelling studies (Massonnet et al., 2013; Holland et al., 2014; Zhang, 2014), the changes in the Ross and BA Seas are less clear. The interpretation of the trends in SIV in the Ross and BA Seas is complicated by the pronounced spatial heterogeneity of the local trends in sea ice thickness (Holland et al., 2014).

3.1.3. Sea ice drift and speed

To compute the mean ice speeds shown in Figure 6, we follow the method of Tandon et al. (2018). This method uses daily ice drift vector components to include sub-monthly variations in the ice drift direction. These variations have a non-negligible impact on the monthly mean ice speeds (Docquier et al., 2017; Tandon et al., 2018) as the timescale for changes in the sea ice drift direction is on the order of 5 days (Rampal et al., 2009). In the Northern Hemisphere, the means are further restricted to the Central Arctic, avoiding coastal areas within 150 km of the shore (see Figure 1 of Tandon et al. (2018)). This spatial domain aims to be representative of the ice drift in the Arctic ice pack. Sea ice in the Southern Ocean is essentially seasonal. Therefore, we only exclude coastal areas within 150 km of the coast to compute the mean ice speed in the Antarctic. Lastly, the means from the two model runs are for regions where the ice concentration is at least 15 %.

Observations from the International Arctic Buoy Programme (IABP) show a seasonal maximum in mean sea ice speeds in September-October when

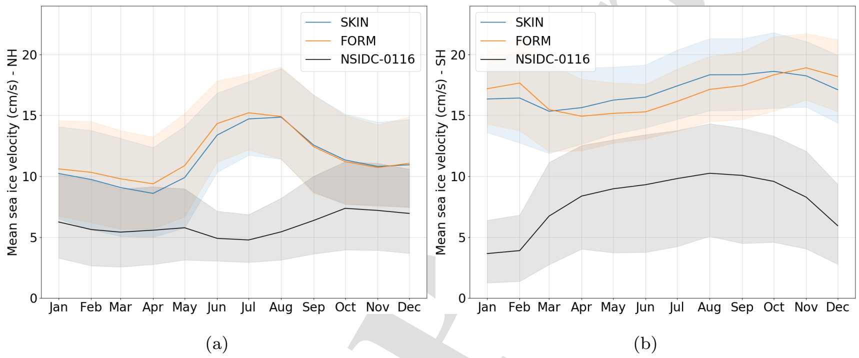

Figure 6: Same as in Figure 2 but for the mean sea ice drift speed ($\|\vec{u}_i\|$, in cm/s) in the Northern (6a) and Southern (6b) Hemispheres. The continuous black line corresponds to the means from the NSIDC-0116 product. The mean ice drift speeds are calculated from the daily sea ice drift vector components following Tandon et al. (2018) in the Arctic and 150 km off the coast in the Antarctic. The means from the FORM and SKIN runs are further restricted to areas with at least 15 % sea ice concentration. Shaded areas are enclosed by the lowest 10^{th} and highest 90^{th} percentiles of the mean sea ice speeds from the SKIN run (blue), FORM run (orange) and NSIDC-0116 product (black).

sea ice is thinner (Olason and Notz, 2014). This seasonality is barely seen in the NSIDC-0116 observational product (Figure 6a). This NSIDC-0116 bias is linked to the large uncertainties occurring during the melt season in the measured sea ice drift (Sumata et al., 2015). NEMO-LIM3 simulates a seasonal maximum in sea ice speed in July–August, when the simulated ice pack tends to a free drift state (Figure 6a). The timing of the minimum in Arctic SIA from NEMO-LIM3 is likely responsible for such a difference with the IABP observations. The simulated minimum in mean ice speed occurs in April when sea ice is seasonally thickest.

The general shapes of the seasonal cycles of Figure 6a comply with the past study of Docquier et al. (2017), albeit the magnitudes of the mean ice speed are higher in our FORM and SKIN runs than in that study. As for Docquier et al. (2017), our configuration of NEMO-LIM3 overestimates the mean sea ice speeds from the NSIDC-0116 product in the Arctic. In the Antarctic, the ratio of the winter mean sea ice speeds from NEMO-LIM3 and the NSIDC-0116 product is close to the meridional sea ice drift correction coefficient of Haumann et al. (2016). Barthélemy et al. (2017) reported, during the austral summer, lower mean Antarctic ice speeds than in our simulations (Figure 6b). We find a significant effect of sub-monthly variations in the ice drift direction on the mean ice speed in the Southern Ocean, particularly in summer when sea ice is close to a free drift state. These effects explain many differences between Figure 6b and the mean seasonal ice speeds detailed by Barthélemy et al. (2017).

NEMO-LIM3 produces a realistic spatial distribution of the annual mean ice drift in the Arctic (Figure 7a). The spatial extent of the Beaufort Sea

Gyre in the FORM run is smaller than in the NSIDC-0116 product (Figure 7c). The simulated transpolar ice drift follows a path closer to the northern coast of the CAA and Greenland than the observations. However, the spatial distribution of the modelled ice drift is in line with other CMIP3 and CMIP5 models in the Arctic (Kwok, 2011; Tandon et al., 2018).

Three main atmospheric lows control the three major sea ice drift gyres around Antarctica (Kwok et al., 2017). The Amundsen Sea Low drives the Ross Sea Gyre, and the sea ice exports to the open ocean around 180 °S. The Riiser Larsen Sea Low at 30 °E connects to the Weddell Sea Gyre. The Davis Sea Low steers the cyclonic ice motion around 90 °E. NEMO-LIM3 reproduces these three main ice drift gyres around Antarctica (Figure 7b). The simulated ice drift near the coast of East Antarctica is higher than in the NSIDC-0116 product (Figure 7d). Additionally, the simulated sea ice drift in most of the MIZ of the Southern Ocean underestimates the northward component of the observed ice drift. This underestimation extends to the interior of the sea ice cover in the Atlantic and Pacific sectors of the Antarctic.

The modelled trends in the annual mean Arctic ice drift speed underestimate the observed trend in this quantity from the NSIDC-0116 product (Table 3) and other studies (Rampal et al., 2009; Tandon et al., 2018; Lipatov et al., 2021). This underestimation is present in other CMIP5 models and accentuates in summer (Tandon et al., 2018). In the Southern Hemisphere, surface winds have intensified over the past decades leading to an acceleration of the sea ice drift (Zhang, 2014). Regional changes in surface winds drive the trends in the sea ice drift in the Southern Ocean (Kwok et al., 2017). The FORM run captures the positive trends in the annual mean ice drift speed in

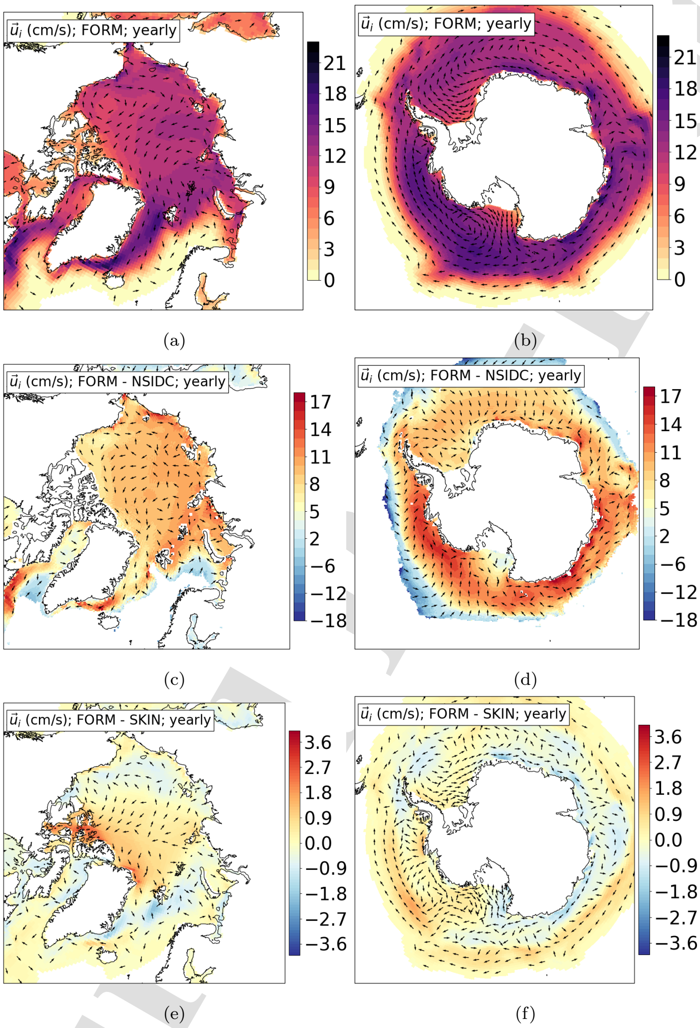

Figure 7: Annual mean sea ice drifts ($\vec{u}_i$, in cm/s) from the FORM run (7a, 7b) and differences in the annual mean sea ice drift from the FORM run and the NSIDC-0116 product (7c, 7d) and from the FORM and SKIN runs (7e, 7f) in the Northern (7a-7e) and Southern (7b-7f) Hemispheres over 1980–2019. The arrows show the direction of the vectors. Note the distinct colour scales to compare the FORM run with the NSIDC-0116 product and the reference SKIN run.

the Ross and Weddell Seas. These two regions of the Southern Hemisphere are crucial for sea ice dynamics. The simulated trends in the FORM run are not statistically significant in other areas of the Antarctic (Table 3).

Table 3: Trends in the annual mean ice drift speed (cm/s per decade) over 1987–2019 in the Northern and Southern Hemispheres as well as specific regions of the Antarctic. The regions are defined in Table 1. Yearly mean ice drift speeds are calculated from the daily sea ice drift vector components and 150 km off the coast. The spatial averaging domain is further restricted in the Northern Hemisphere following Tandon et al. (2018). The annual mean ice speeds from the FORM and SKIN runs are calculated in the presence of at least 15 % sea ice concentration.

	NH	SH	Weddell	BA Seas	Ross	Pacific	Indian
FORM	-0.07	**0.12**	**0.35**	0.05	**0.11**	-0.03	-0.11
SKIN	**0.38**	**0.09**	**0.25**	0.12	0.05	0.04	**-0.22**
NSIDC-0116	**0.66**	**0.38**	**0.22**	**0.64**	**0.46**	**0.37**	**0.62**

In either hemisphere, the formulation of the ANDC and ONDC leads to only minor differences in the seasonal climatology of the mean ice drift speed in the ice pack (Figure 6). The impact of the form drag is small on the direction and magnitude of the annual mean ice motion vectors (Figures 7e and 7f). This small impact complies with the past results from Castellani et al. (2018). The relative differences in the yearly mean ice speeds are less than 10 % in the Central Arctic and Antarctic ice pack. The representation of the trend in Arctic sea ice drift speeds degrades compared to the observations when including form drag (Table 3). The differences in the regional trends in this diagnostic suggest a long-term effect of the form drag on the sea ice drift. We advise examining this form drag effect jointly with the ice strength parameterization (e.g., Chikhar et al. (2019)).

3.2. Form drag over sea ice

3.2.1. Total atmospheric and oceanic neutral drag coefficients

The seasonal cycles of the mean ANDC and ONDC from the FORM run share some common properties between the Northern and Southern Hemispheres (Figure 8). The mean neutral drag coefficients are maximum during the melt season and minimum during freezing months. The seasonality of the mean ANDC and ONDC are nearly symmetrical because of the formulation of the individual form drag contributions. The contribution from melt pond edges is the only term in the formulation of the form drag without effects on the ONDC.

The spatial distributions in the Arctic of the annual mean ANDC (Figure 9a) and ONDC (Figure 9b) are related to the sea ice thickness (Figure 5a). Indeed, Arctic regions with thicker sea ice tend to have higher neutral drag coefficients than other regions with thinner sea ice in winter (Martin et al., 2016). The spatial distributions in the Antarctic of the annual mean ANDC (Figure 9c) and ONDC (Figure 9c) confirm this correspondence with the sea ice thickness (Figure 5b). In the Southern Hemisphere, the neutral drag coefficients are highest in the BA Seas and parts of the Ross and Weddell Seas where sea ice is also thickest on average.

In-situ measurements of the ANDC fluctuate highly following the region, the time of the year and the surface aspect of sea ice (Guest and Davidson, 1991; Andreas et al., 2010). ANDC are approximately 1.2×10^{-3} to 3.1×10^{-3} over first-year ice, 1.1×10^{-3} to 2.7×10^{-3} in the MIZ, and 1.2×10^{-3} to 6.7×10^{-3} over multiyear ice (MYI) (Guest and Davidson, 1991;

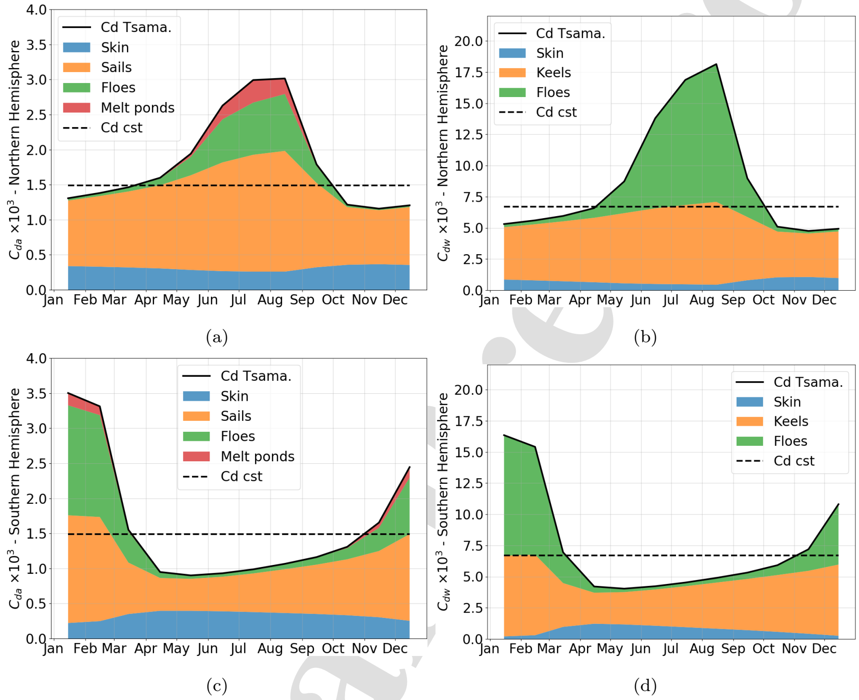

Figure 8: Seasonal cycles of the mean (1980–2019) neutral drag coefficients (black) and the form drag contributions associated with surface skin (blue), sails and keels (orange), floes (green) and melt ponds (red) in the Northern (8a, 8b) and Southern (8c, 8d) Hemispheres at the atmosphere-ice (8a, 8c) and ocean-ice (8b, 8d) interfaces from the FORM run. Dashed horizontal lines in black indicate the value of the constant drag coefficients from the SKIN run. The means are multiplied by the constant factor of 10^3 and are weighted by the ice concentration where the ice concentration is at least 15%.

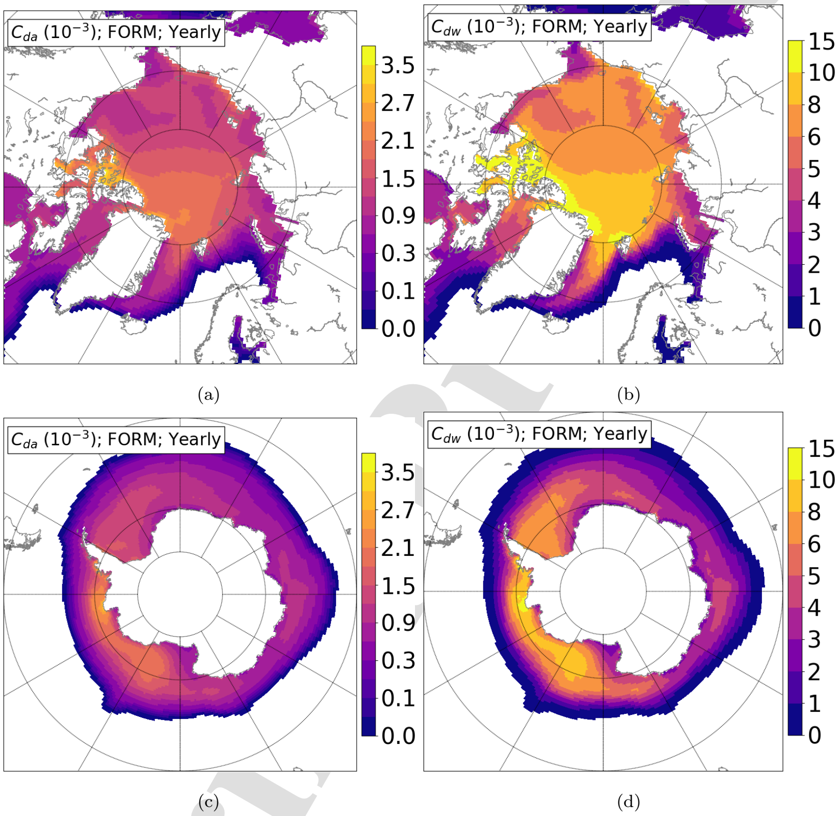

Figure 9: Annual mean values (1980–2019) of the atmospheric neutral drag coefficient (C_{da}) (9a, 9c) and oceanic neutral drag coefficient (C_{dw}) (9b, 9d) in the Northern (9a, 9b) and Southern (9c, 9d) Hemispheres. The coefficients are expressed using 10^{-3}.

Schröder, 2003). Moreover, the spatial and temporal variability of the ANDC is high (Castellani et al., 2014; Cole et al., 2017; Heorton et al., 2019). Petty et al. (2017) produced pan-Arctic estimates of the ANDC for early spring by combining observations from IceBridge topography data and existing form drag parameterizations (Garbrecht et al., 2002; Lüpkes et al., 2012; Castellani et al., 2014). These estimates correspond to those simulated in the Arctic in the FORM run (Figure 9a).

The canonical value for the ONDC is usually 5.5×10^{-3}, based on measurements collected in the Beaufort Sea during the AIJDEX campaign (McPhee, 1980). This value is more representative of winter sea ice conditions and MYI sea ice floes. In general, ONDC observations are restricted to certain sea ice conditions for safety and logistical reasons. This makes comparisons between observations and model results challenging. In the FORM run, the December-January-February mean ONDC in the Beaufort Sea varies between 3×10^{-3} and 5×10^{-3}. The constant ONDC used in the SKIN run is 6.71×10^{-3}. This constant represents the global mean ONDC weighted by the sea ice concentration when including form drag in our model setup. Past observations of the ONDC fall within the range of 1×10^{-3} to 20×10^{3}. Some estimates exceed this range in the Beaufort, Greenland and Bering Seas (Shirasawa and Ingram, 1991; Lu et al., 2011). More recent ONDC estimates confirm this range of values for the ONDC (Shaw et al., 2008; Cole et al., 2014; Randelhoff et al., 2014; Cole et al., 2017; Kim et al., 2017; Dewey, 2019; Heorton et al., 2019). Therefore, the simulated ONDC is within the observational uncertainty and is of the same order as the ONDC canonical value of McPhee (1980).

The values of the ANDC and ONDC from the FORM run are in relatively good agreement with those from existing pan-Arctic modelling studies (Tsamados et al., 2014; Martin et al., 2016; Castellani et al., 2018; Chikhar et al., 2019). The spatial differences in neutral drag coefficients between these studies and the FORM run may arise from differences in the representation of the sea ice state. The magnitudes of the winter mean ANDC (1.25×10^{-3}) and ONDC (5.0×10^{-3}) simulated in the FORM run are close to those from Tsamados et al. (2014). Modelling studies (Tsamados et al., 2014; Chikhar et al., 2019; Castellani et al., 2018) report various summer mean neutral drag coefficients in the Arctic. The summer mean ONDC from the FORM run for the Arctic regions is closer to the results of Martin et al. (2016) and Chikhar et al. (2019). The mean of the variable ANDC compares better with the study of Tsamados et al. (2014). These various mean neutral drag coefficients suggest uncertainties in current parameterizations of the drag coefficients during the melt season, as stated by Brenner et al. (2021).

The annual mean ANDC and ONDC from the FORM run experience negative trends in the Arctic except locally in the Chukchi Sea (Figures 10a and 10b). The spatial distribution of these trends is consistent with the model results of Tsamados et al. (2014). Martin et al. (2016) showed negative trends in the mean Arctic ONDC in winter but positive ones in summer. In the FORM run, the trends in the Arctic neutral drag coefficients strengthen during summer but do not change sign seasonally. In the Southern Hemisphere, the trends in the annual mean ANDC (Figure 10c) and ONDC (Figure 10d) are regional and statistically significant only in the western sector of the

Antarctic. The FORM run presents positive trends in the neutral drag coefficients in the Ross Sea but negative trends in these coefficients in the BA Seas.

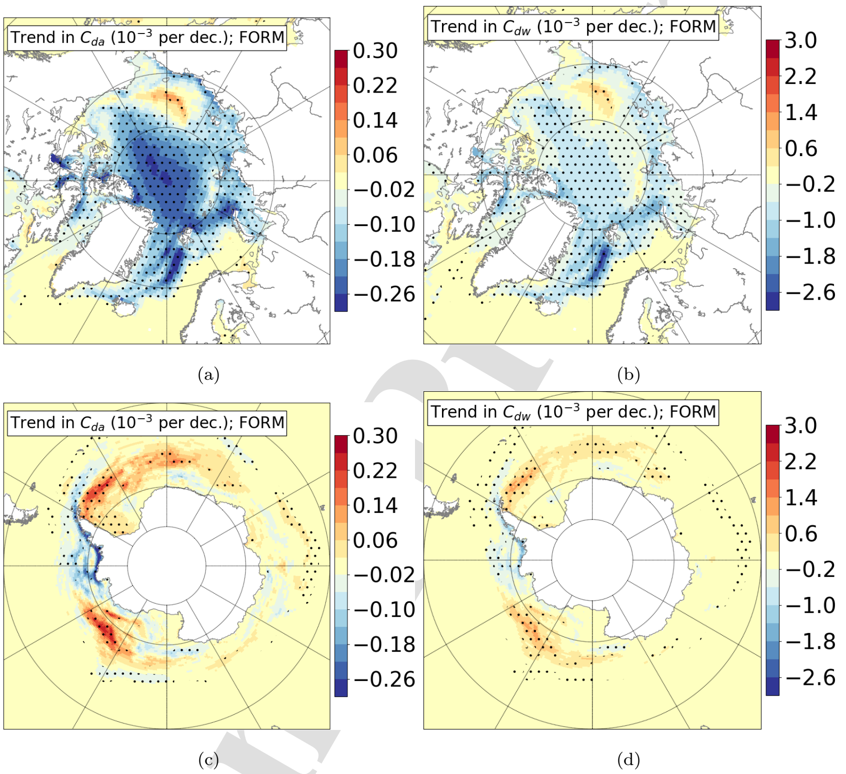

Figure 10: Trends (1980–2019) in the annual mean ANDC (10a, 10c) and ONDC (10b, 10d) in the Northern (10a, 10b) and Southern (10c, 10d) Hemispheres expressed in 10^{-3} per decade. Dots indicate a p-value less than 0.1.

According to Brenner et al. (2021), numerical studies using the form drag formalism of Tsamados et al. (2014) simulate a maximum in the mean

Arctic ONDC during summer (Tsamados et al., 2014; Martin et al., 2016; Chikhar et al., 2019) in contrast with observations in the Beaufort Sea of a seasonal minimum in late summer and early fall. The observed ONDCs in the Beaufort Sea by Brenner et al. (2021) are principally driven by the form drag contribution associated with ice keels rather than floe edges, in summer. This contrasts with Figure 8b which shows the opposite for the Arctic ice pack. Equation 1 underestimates the mean floe length in most of the Arctic regions (Bateson, 2021). As a result, the seasonality of the modelled neutral drag coefficients in the Arctic (Figures 8a and 8b) are likely overestimated in summer due to excessive contributions from floe edges. In the Southern Ocean, floes have smaller sizes, notably for Antarctic sea ice being surrounded by the ocean and thus exposed to the action of waves. Thus, the underestimation of the mean floe length by Equation 1 is probably more limited in Antarctic than in the Central Arctic. Furthermore, $\beta = 0.5$ selected for this study is closer to the suggested value of 0.3 for the Antarctic and Western Fram Strait (Lüpkes et al., 2012). The sensitivity of the neutral drag coefficients to the contribution of floe edges will be discussed in further details in Section 3.2.3.

Observations strongly suggest that our currently used bulk formulation (Equation 6) overestimates the oceanic heat flux in spring when sea ice melt re-stratifies the upper ocean (Peterson et al., 2017). However, the ocean stability question remains a challenge for observational studies (McPhee, 1992; Cole et al., 2017). In addition, we have considered the case for atmospheric neutral stratification over sea ice only, despite the importance of the atmospheric stability for the atmosphere–ice turbulent fluxes (Lüpkes and

Gryanik, 2015). Accounting for the ocean and atmosphere stability effects should be the focus of future model studies.

3.2.2. Contributions associated with sails and keels

The contributions from sails and keels are a function of the height-to-distance ratios of sails (H_s/D_s) and keels (H_k/D_k), which derive from the deformed ice volume (V_{rdg}) and area fraction (A_{rdg}). The greater the deformed ice volume over the deformed ice area (V_{rdg}/A_{rdg}), the greater the aspect ratios of sails and keels, and the higher the form drag contributions from sails and keels. Thus, regions exhibiting heavily ridged sea ice tend to have higher form drag contributions associated with sails and keels than areas with thinner and more levelled sea ice. In the FORM run, the model simulates thick and highly deformed MYI in the western sector of the Arctic (Figure 11b). This sea ice transits from the Central Arctic to the Greenland Sea through Fram Strait. In these regions, the simulated contribution of sails and keels to the neutral drag coefficients is higher than in the other areas of the Arctic. These results are in line with other modelling studies (Tsamados et al., 2014; Martin et al., 2016; Castellani et al., 2018).

Antarctic sea ice is more seasonal, thinner and less deformed than in the Arctic. Thus, the annual means of the form drag contributions from sails and keels are sensibly smaller in the Southern Hemisphere, except in the BA Seas and parts of the Ross and Weddell Seas (Figure 11f). In the latter regions, sea ice dynamical processes are more active and yield larger volumes of deformed ice. The contributions of sails and keels are more moderate in the Antarctic MIZ because of small sea ice concentrations.

In the FORM run, the contributions of sails and keels are essential for

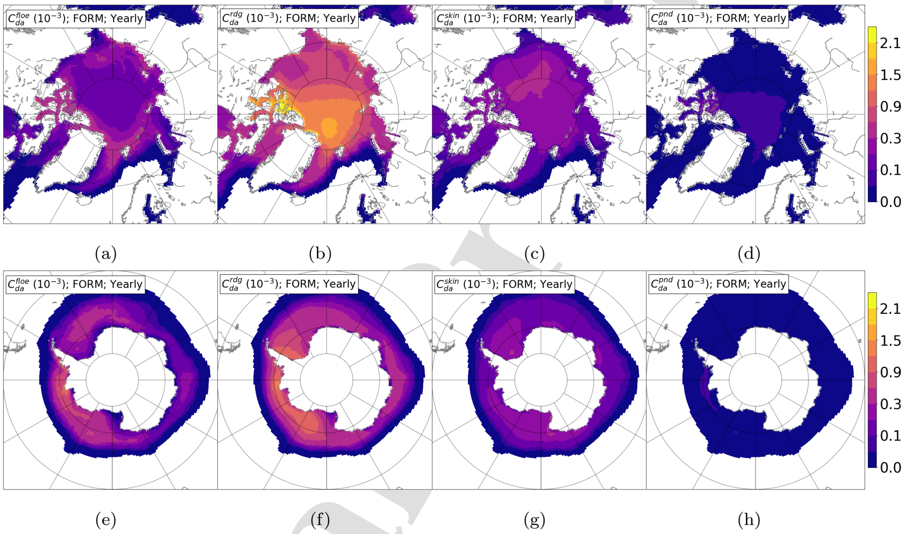

Figure 11: Annual mean (1980–2019) form drag contributions to the ANDC associated with floe edges (11a, 11e), surface sails (11b, 11f), upper surface skin drag (11c, 11g) and melt pond edges (11d, 11h) in the Northern (11a-11d) and Southern (11e-11h) Hemispheres. The coefficients are expressed using 10^{-3}.

the monthly mean ANDC and ONDC in winter (Figure 8). The means of these contributions are maximum in summer because of seasonal changes in the simulated volume fractions of deformed ice. In our simulations, sea ice after melting is principally composed of ridged ice that has shifted from thick to thinner ice categories. Thus, the simulated height-to-distances ratios of sails and keels tend to be higher in summer due to large volume fractions of deformed ice.

The annual means of the form drag contributions from sails and keels to the total neutral drag coefficients have significantly decreased in the Arctic over the past decades (-0.12×10^{-3} per decade for C_{da}^{rdg} and -0.40×10^{-3} per decade for C_{dw}^{rdg}). These changes are linked to the loss of the volume fraction of Arctic MYI (Kwok, 2018) and the decline in the volume fraction of deformed ice. The latter drives the negative trends in the aspect ratios of sails and keels (Martin et al., 2016). Indeed, the SIV and the MYI fraction in the Arctic reduced during the satellite era (Kwok, 2018). The decline in the fraction Arctic of MYI is consistent with the decrease in the ratio of the deformed ice volume over the deformed ice area simulated by NEMO-LIM3.

In the Southern Hemisphere, local trends in the annual mean deformed ice fraction lead to regional trends in the sail and keel contributions to the neutral drag coefficients. The latter is positive in the Weddell Sea (0.04×10^{-3} per decade for C_{da}^{rdg} and 0.22×10^{-3} per decade for C_{dw}^{rdg}) and the northern part of the Ross Sea but negative in the BA Seas (-0.05×10^{-3} per decade for C_{da}^{rdg} and -0.18×10^{-3} per decade for C_{dw}^{rdg}). In the Indian and Pacific sectors of the Southern Ocean, the changes in the annual mean deformed ice volume and area fractions are close to zero. Consequently, the sails and keels have no significant impact on the changes in form drag over the past decades in these regions.

3.2.3. *Contributions associated with floe edges*

In the FORM run, the contributions from floe edges to the ANDC and ONDC are prevalent during the summer months (Figure 8). The seasonal maximum in the contributions due to floe edges represent 27 % and 42 % of the total ANDC in the Northern and Southern Hemispheres, respectively. The equivalent contributions at the ocean-ice interface amount to 60 % of the ONDC in summer in either hemisphere. Observations in the Beaufort Sea (Brenner et al., 2021) and model evidence in the Arctic (Bateson, 2021) indicate that Equation 1 poorly represents the mean floe length especially in summer. Due to the definition of the form drag coefficients, the bias in the prescribed floe length likely impacts both the ANDC and ONDC. In winter, the effects of floe edges on the neutral drag coefficients are restricted to the MIZ, which we expect from the lesser fraction of open water in the ice pack. The contributions of floe edges to the neutral drag coefficients have only a weak signature on the mean ANDC and ONDC in winter.

To examine the sensitivity of the modelled neutral drag coefficients to the prescribed floe length, we make use of the sea ice conditions from the FORM run and the formalism of Tsamados et al. (2014) to calculate the form drag coefficients. Using this approach, we determine that prescribing a constant floe length of 300 m reduces the ANDC and ONDC in the Arctic to 2.3×10^{-3} and 7.7×10^{-3} in August, respectively, thereby almost suppressing the summer peak seen in Figures 8a and 8b. This confirms the conclusions of Bateson (2021). In practice, setting $L_f = 300\,\mathrm{m}$ is equivalent to suppressing the form drag contribution associated with floe edges, as this horizontal length largely exceeds the vertical height of floe edges. When varying β from 0.5 to 1.5 in Equation 1, the seasonal peak in the ANDC (ONDC) is decreased by 10 % (25 %) but the shape of the peak is maintained. The existence of such peak arises from definition of the floe length parameterization (Equation 1). This parameterization returns relatively small floe lengths as soon as sea ice concentration deviates from unity ($A < 0.8$). The seasonality of the modelled form drag contribution of floe edges in the Arctic needs to be re-evaluated with a more realistic formulation for floe sizes.

The overestimation in summer of the form drag contribution associated with floe edges in the Arctic raises doubts for the representation of this contribution in the Southern Ocean. Similarly to the Arctic, setting a constant floe length of 300 m nearly suppresses the form drag contribution of floe edges, when calculating form drag with sea ice conditions from the FORM run. However, floes have smaller lengths in the Southern Ocean than in the Arctic Basin (Roach et al., 2018). Thus, floe edges are likely to be more important to form drag in the Antarctic than the Arctic. Changing β from 0.5 to 1.5 in Equation 1 decreases the ANDC and ONDC to 3.1×10^{-3} and 14.0×10^{-3}, respectively, in the Southern Ocean. Despite of the uncertainty in the mean floe length formulation, the seasonal peak in the Antarctic neutral drag coefficients is maintained by the contribution from surface ridges (Figure 8c and 8d). Consequently, the uncertainty in the floe length parameterization impacts the magnitude of the summer maximum in neutral drag coefficients but not the existence of this seasonal maximum.

The freeboard-to-floe-length (H_f/L_f) and draft-to-floe-length (H_d/L_f)

ratios (hereafter referred to as aspect ratios of floe edges) control the spatial distribution of the form drag coefficients due to floe edges (Figure 11a). The aspect ratios of floe edges are high in the Arctic MIZ, the CAA, and the northern coast of Greenland. In these regions, the small sea ice concentrations, and thus the short mean floe lengths, lead to a strong influence of the freeboard and draft of sea ice on the aspect ratios of floe edges. On the opposite, the aspect ratios of floe edges are low in the Arctic ice pack because of large floes.

As in the Arctic, the aspect ratios of floe edges drive the annual mean contribution from floe edges to the ANDC in the Southern Ocean (Figure 11e). Thick sea ice in the BA Seas, Ross, Weddell and the Davis Seas (90 °E) are associated with higher aspect ratios of floe edges. Except in the Ross Sea, floe lengths are maximum close to the coast of Antarctica and decrease northwards with sea ice concentration. The spatial maximum along the coast of Antarctica strongly inhibits the effect of floe edges on the ANDC and ONDC in this area.

The trends in the annual mean form drag contribution from floe edges to the total neutral drag coefficients are not statistically significant when averaged over the Arctic or the regions of the Antarctic. The lack of statistical significance in these trends takes its origin from the variability in the freeboard-to-floe-length and draft-to-floe-length ratios. In consequence, the spatial trends in the ANDC and ONDC displayed in Figure 10 may not be explained by changes in the contribution associated with floe edges. We may anticipate a greater influence of floe edges on the total form drag in the Arctic in future decades, as Arctic sea ice is transitioning to a more seasonal state.

3.2.4. *Surface skin drag*

The skin drag coefficients are the second contribution in order of importance to the seasonal cycle of the ANDC and ONDC during winter (Figure 8). The skin drag contributes to the ANDC (ONDC) when the distance between sails (keels) is less than twenty (ten) times the vertical height of sails (keels) (Tsamados et al., 2014). These conditions are satisfied in autumn and onward in winter when the density of sails and keels decreases due to the formation of levelled sea ice through thermodynamical processes. In summer, sea ice melt generates a decrease in the volume fraction of deformed ice leading to a higher density of sails and keels. These changes diminish the overall contribution of surface skin to the neutral drag coefficients in summer.

The maps of the annual mean surface skin drag coefficients in the Arctic (Figure 11c) and Antarctic (Figure 11g) show that the spatial distribution of this coefficient is relatively homogeneous compared to other form drag contributions. We expect a small spatial variability of the skin drag coefficients in the ice pack because these coefficients aim to represent the drag effect of levelled ice.

3.2.5. *Contribution associated with melt pond edges*

Melt ponds appear over sea ice when the surface meltwater and precipitation collect in the depression of the ice cover. In the Arctic, the mean melt pond area fraction of sea ice reaches a maximum of 38 % in July in the SKIN and FORM runs (see Sterlin et al. (2021)). This represents a form drag contribution of 10 % of the Arctic ANDC. In the Antarctic, melt ponds are mainly non-existent because of different snow and ice surface thermodynamical processes. Recent observations from cruise ships suggest that the effect of melt ponds in the Antarctic may be more substantial than previously thought (Istomina, 2020). For this reason, the melt pond scheme remains active in the Southern Hemisphere in our model version of NEMO-LIM3.

The melt pond area fraction simulated in the Southern Hemisphere is non-negligible even though the snow and ice surface melt fluxes are small and the available meltwater for ponding is little. The misrepresentation of melt ponds in the Southern Hemisphere arises from the redistribution of meltwater among the ice thickness categories by the melt pond scheme. The scheme distributes the volume of meltwater over thin ice categories first. These categories extend over large areas in the Antarctic due to more seasonal and less deformed sea ice compared to the Arctic. As a result, the simulated melt ponds are shallow ($\sim$5 cm depth) but cover large areas ($\sim$20 % ponded ice area) in the Southern Hemisphere. Thus, the effect of melt ponds on the surface albedo is weak. The impact of melt ponds on the form drag may be more problematic. The mean contribution of melt pond edges represents up to 6 % of the total ANDC in the Southern Hemisphere.

The trend in the form drag contribution associated with melt pond edges is negative in the Arctic in summer. In our current implementation of the melt pond scheme, the refreezing mechanism of melt ponds impacts the trends in the melt pond area fractions in the Arctic (Sterlin et al., 2021). This mechanism is adjusted to decrease the melt pond volume when the ice surface temperature is less than $-0.15\,^{\circ}$C and to match current observations. The trend in the mean Arctic melt pond area fraction of sea ice during June-

July-August is 3.13 % per decade in the FORM run. Despite this positive trend, the aspect ratio of melt pond edges is reducing in summer because of smaller freeboard height. In turn, the negative trend in the aspect ratio of melt pond edges drives the decline in the contributions of melt ponds to the ANDC.

3.3. Impact on the ocean surface properties

3.3.1. Ocean surface stress

In the presence of sea ice, the formulation of the neutral drag coefficients modulates the effect of surface winds and sea ice drift on the ocean surface stress. The constant ANDC (ONDC) over sea ice makes the wind (ocean) surface stress in ice-covered areas directly proportional to the square of the relative surface wind (sea ice drift) speeds. In high latitudes, surface wind speeds are higher in winter than in summer because of more frequent and intense storms. Therefore, the simulated ocean surface stress in the ice pack is more important in winter than in summer when selecting constant drag coefficients over sea ice (Barthélemy et al., 2017). On the other hand, the variable ANDC and ONDC over sea ice break this direct relation between surface stress and relative wind or ice velocities (Martin et al., 2016). In the FORM run, the ocean surface stress under sea ice is maximum in summer (Figures 12b, 12c) despite low surface wind speeds. This stress is minimum in winter when surface wind speeds are higher (Figures 12a, 12d).

The reversal of the ocean surface stress seasonality when including form drag compared to constant drag coefficients is principally dictated by the mean seasonal cycles of the neutral drag coefficients (Figure 8). Figure 13 further illustrates the seasonality differences in ocean surface stress between

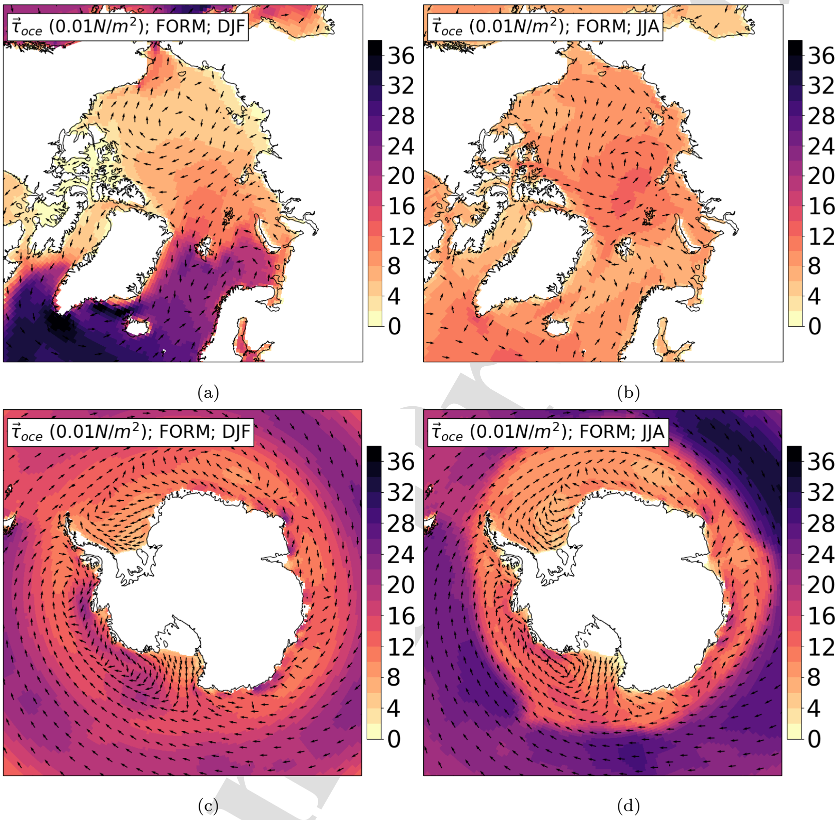

Figure 12: Seasonal mean (1980–2019) ocean surface stress ($\vec{\tau}_{oce}$) (0.01 N/m^2) from the FORM run in December-January-February (DJF) (12a, 12c) and June-July-August (JJA) (12b, 12d) in the Northern (12a, 12b) and Southern (12a, 12d) Hemispheres. The arrows show the direction of the vectors.

the two simulations. The anti-cyclonic ocean surface stress driving the Beaufort Sea Gyre intensifies in summer and lessens in winter with form drag. In the SKIN run, this ocean surface stress is minimum in summer and maximum in winter (Figures 13a, 13b). In addition, the FORM run shows higher mean ocean surface stresses than the SKIN run in Fram Strait and the Central Arctic in both summer and winter. Correspondingly, the variable ANDC and ONDC in these regions are higher than the constant drag coefficients used in the SKIN run all year round. In the Southern Hemisphere, the ANDC and ONDC from the FORM run strengthen the ocean surface stress steering the Weddell and the Ross Sea Gyres during summer (Figures 13c). In winter, the ocean surface stress decreases in the FORM run compared to the reference SKIN run (Figures 13c).

We anticipate that our model configuration overestimates the effect of form drag on the ocean surface stress in summer, because of the misrepresentation of the form drag contribution associated with floe edges. The sensitivity of the modelled ocean surface stress to the contribution of floe edges may be investigated using the sea ice conditions and ocean surface state simulated in the FORM run. This method is equivalent to varying parameters in the form drag parameterization and assuming negligible effects on the sea ice state and ocean surface velocities. While the impact of form drag on the sea ice concentration is limited, the effects on the ice thickness and relative ice velocity are more significant. Thus, this method allows only a qualitative assessment of the modelled ocean surface stress sensitivity. In the Arctic, we determine that prescribing a constant floe length of 300 m removes the reversal of seasonality in ocean surface stress. Varying β from

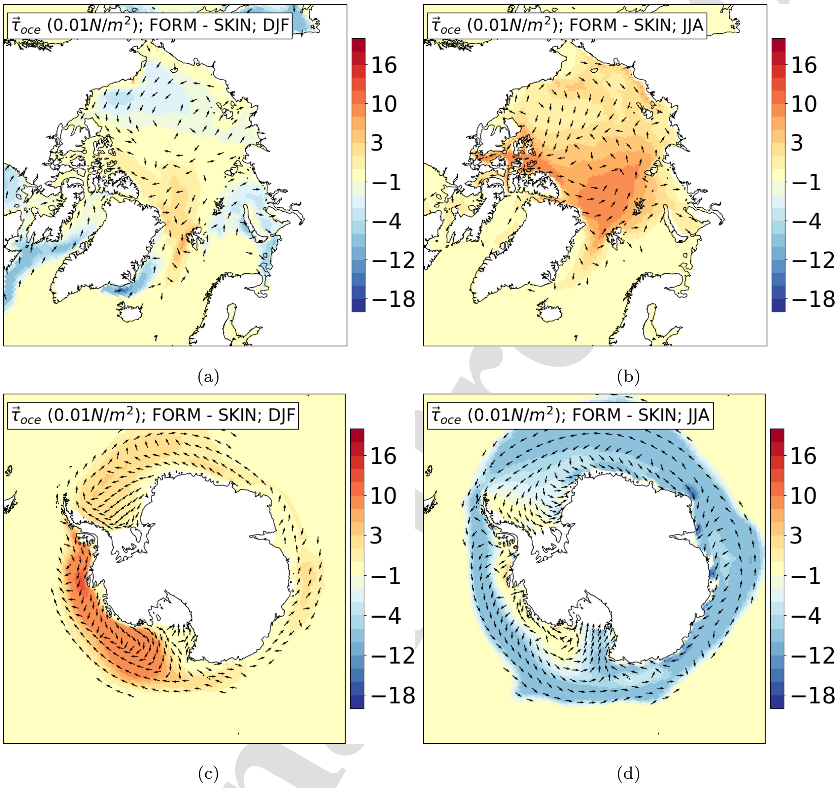

Figure 13: Differences in seasonal mean (1980–2019) ocean surface stress ($\vec{\tau}_{oce}$) (0.01 $\mathrm{N/m^2}$) between the FORM and SKIN runs in December-January-February (DJF) (13a, 13c) and June-July-August (JJA) (13b, 13d) in the Northern (13a, 13b) and Southern (13c, 13d) Hemispheres. The arrows show the direction of the vectors. The vectors with a magnitude close to zero are masked.

0.5 to 1.5 decreases the summer maximum in the mean Arctic ocean surface stress by $0.02\,\mathrm{N/m^2}$. These results are in line with the suppression of the seasonal maximum in ONDC when prescribing a constant floe length of 300 meter, and the decreased seasonal maximum in ONDC when increasing β. In the Antarctic, prescribing a constant floe length of 300 meter or varying β modify the magnitude of the maximum in ocean surface stress during the austral summer. Nevertheless, this seasonal maximum is calculated even without the contributions from floe edges, due to the contribution from ice keels.

In our setup, the model computes the heat and momentum fluxes at the ice–ocean interface using the ice velocity relative to the ocean surface velocity. This method enables the representation of the negative feedback between the Ekman pumping and the relative surface velocities in polar ocean gyres, namely, the ice-ocean stress governor mechanism (Meneghello et al., 2018, 2020). When a polar ocean gyre driven by surface stress spins up, the ice velocity equalizes with the ocean surface velocity, turning off the surface stress. Observational studies exploring the dynamic of the Beaufort Gyre rely on constant drag coefficients for sea ice without form drag (e.g., Meneghello et al., 2017). In our model setup, the curl of the ocean surface stress ($\vec{\nabla} \times \vec{\tau}_{oce}$) shows evidence of a form drag effect on the Ekman pumping in polar oceans, especially in summer (not shown). Form drag enhances the downwelling in the Beaufort Gyre in summer but reduces it in winter. While the magnitude of the downwelling is likely biased by the prescribed mean floe length during summer, we may have more confidence in the modelled upwelling during winter. In the Southern Ocean, form drag leads to a more efficient downwelling along the coastline of Antarctica and a larger upwelling in the ice pack during the melt season. As for the Arctic regions, the seasonal peak in neutral drag coefficients enhances the momentum fluxes between the ocean and sea ice systems. On the other hand, form drag reduces the efficiency of the Ekman pumping under Antarctic sea ice in winter. We advise investigating Ekman pumping rates with a variable formulation of the neutral drag coefficient and a more accurate floe size formulation than Equation 1.

The simulated interdecadal trends in the annual mean ocean surface stress exhibit stark contrasts in the ice pack depending on the formulation of the ANDC and ONDC in the simulations (Figure 14). The trend in the Arctic ocean surface stress is negative when selecting the parameterization of Tsamados et al. (2014) but positive when using constant neutral drag coefficients (Martin et al., 2016). We confirm this result using our fully coupled ocean–sea ice model. In the FORM run, the trend in ocean surface stress is $-4.94 \times 10^{-3}\,\mathrm{N/m^2}$ per decade in the Arctic ice pack (Figure 14a). The corresponding value in the SKIN run is $0.35 \times 10^{-3}\,\mathrm{N/m^2}$ per decade (Figure 14b).

The formulation of the neutral drag coefficients leads to pronounced regional differences in the simulated ocean surface stress in the western sector of the Antarctic. Notably, the trend in ocean surface stress from the FORM run is positive in the Western Ross Sea and the Weddell Sea but negative in the BA Seas (Figure 14c). In the SKIN run, the annual mean ocean surface stress declined in the Western Ross Sea and increased in the Weddell Sea and the BA Seas (Figure 14d). The simulated trends in ocean surface stress are similar in the eastern sector of the Antarctic.

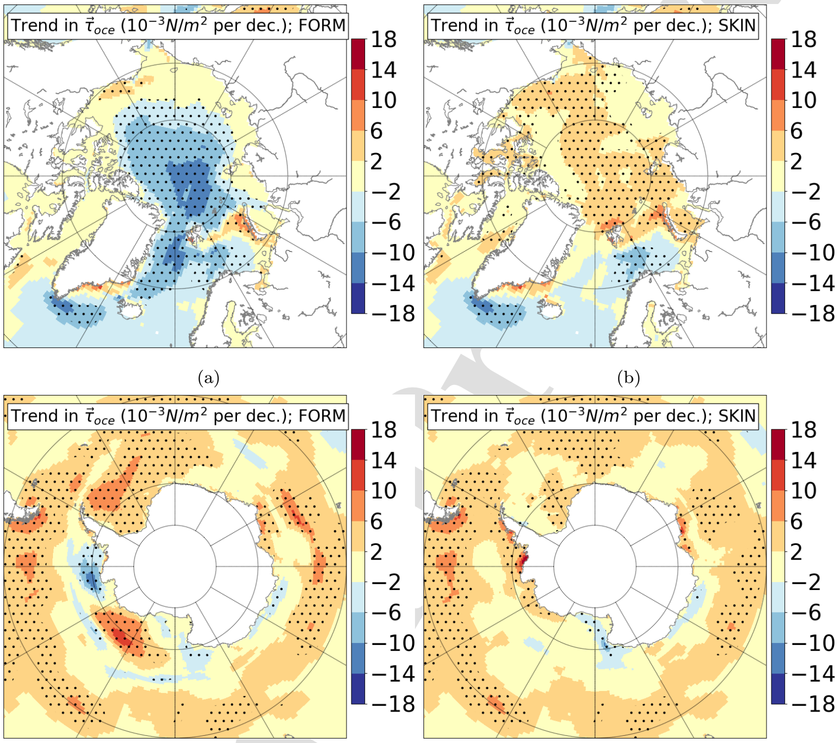

(a) (b) (c) (d)

Figure 14: Trends (1980–2019) in the annual mean ocean surface stress module ($\|\vec{\tau}_{oce}\|$) (10^{-3} N/m^2 per decade) from the FORM (14a, 14c) and SKIN (14b, 14d) runs in the Northern (14a, 14b) and Southern (14c, 14d) Hemispheres. Dots indicate a p-value less than 0.1. The trends are calculated over 1980–2019.

The trends in ANDC and ONDC (Figure 10) are the main drivers of the changes in the annual mean ocean surface stress simulated in the FORM run in polar regions. Indeed, the atmospheric forcing of the two model runs is identical. There are only minor differences in sea ice drift between the FORM and SKIN runs because sea ice dissipates the effect of form drag on the wind stress through mechanical ice deformation. The representation of the sea ice concentration in the FORM run is close to the one in the SKIN run. Therefore, the atmospheric momentum input through the open water fraction is nearly unchanged by form drag. Thus, the changes in ice-ocean surface stress ($\vec{\tau}_{io}$) explain the differences in the total ocean surface stress ($\vec{\tau}_{oce}$) between the two simulations. Consequently, the ONDC controls $\vec{\tau}_{io}$ and subsequently impacts $\vec{\tau}_{oce}$. The modelled trends in the form drag contribution of keels principally explain the trends in ONDC, the trends of the contribution associated with floe edges being not statistically significant.

3.3.2. Sea surface temperature and salinity

The simulated SST under polar ice differs during the melt season and in the MIZ, essentially (not shown). In almost all the Arctic MIZ, the mean June-July-August SST in the FORM run is 0.5 to 1.5 °C higher than in the reference SKIN run. The interior of the Arctic ice cover shows a better agreement between the two simulations in terms of SST. These are close to the freezing point of seawater. In the Arctic MIZ, the differences in the simulated sea ice thickness (Figure 5e) and sea ice concentration (Figure 3f) are spatially co-locating with the differences in SST. The thinner sea ice cover and the less consolidated MIZ simulated in the FORM run allow more heat exchanges between the ocean surface and the atmosphere than in the SKIN run.

The impact of the changes in sea ice properties on the SST concerns also the Antarctic sea ice cover regions. The SST in Antarctic ice-covered areas is generally lower during the austral summer with form drag. This changes in winter when the simulated SST is close to the freezing point of seawater in the two model runs. In the Southern Hemisphere, the sea ice cover tends to be thicker (Figure 5f) and more consolidated (Figure 3f) with the variable neutral drag coefficient formulation. In turn, this hinders the heat exchanges between the atmosphere and the ocean, leading to a lower summer SST in almost all the Antarctic MIZ.

Castellani et al. (2018) reported higher summer mean sea surface temperature in the Arctic MIZ when including form drag in their fully coupled ocean–sea ice model. In their implementation, form drag acts on the transfer coefficient for momentum only, the transfer coefficients for latent and sensible heat fluxes being constant. These authors argue that the warming of the Arctic MIZ is an indirect effect of changes in sea ice properties rather than a direct effect of form drag on the SST. In our implementation, form drag acts on the transfer coefficients for momentum, latent and sensible heat fluxes over sea ice, and the oceanic heat and momentum fluxes under sea ice. However, the impact of form drag on the simulated Arctic SST is close to the one obtained by Castellani et al. (2018). This suggests a similar indirect effect of form drag on the SST through changes in sea ice properties. Form drag impacts the simulated sea ice concentration and thickness. These changes in sea ice properties influence the modelled SST in summer.

The maps of the differences in mean SSS between the FORM and SKIN runs (Figure 15) reveal a net increase in the SSS in most ice-covered areas during summer when activating the form drag scheme. The mean SSS is 0.89 g/kg and 0.52 g/kg higher in summer when using the formulation of Tsamados et al. (2014) in the Arctic and Antarctic, respectively. The increase remains visible in the Central Arctic and the coastal regions of the East Siberian Sea during winter. The SSS in the Beaufort Gyre and the CAA is smaller in the FORM run compared to the SKIN run, except for July and August. In the Southern Hemisphere, the higher summer mean SSS simulated in the FORM run is predominantly observed in the vicinity of the coast and the western regions of the Antarctic. The SSS in the Antarctic MIZ is smaller during summer when using the form drag scheme.

Two mechanisms involving the neutral drag coefficients may explain the higher summer mean SSS simulated when activating the form drag scheme. Firstly, the melting and freezing of sea ice control the seasonality of the SSS in polar regions (Peralta-Ferriz and Woodgate, 2015). Our current implementation of the form drag impacts the turbulent heat fluxes over and under sea ice. These heat fluxes affect the thermodynamics of sea ice and hence the exchange of freshwater between the ocean and ice systems. Secondly, the form drag formalism impacts the ocean surface stress in the ice pack. This stress controls the mixing of the ocean properties in the surface mixed layer, enabling mixing in the upper ocean surface and the underlying water masses.

The net upward ocean surface freshwater flux (F_w) allows investigating the seasonal impact of form drag on the SSS through changes in sea ice melt. F_w includes the mass fluxes associated with evaporation-precipitation, river runoff and the ice-ocean mass fluxes. Although this flux is sensitive

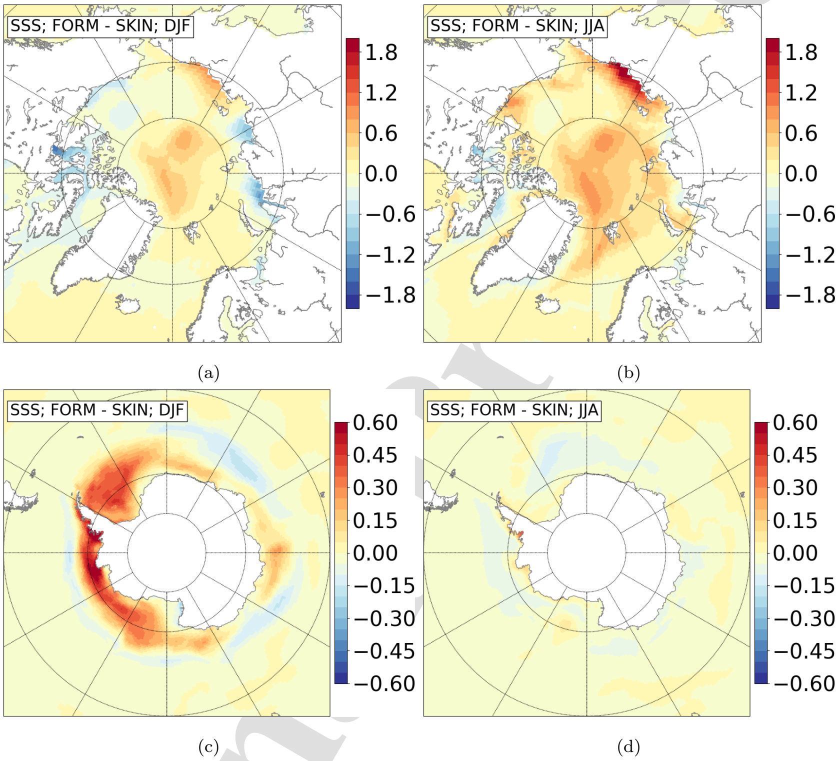

Figure 15: Differences in seasonal mean (1980–2019) sea surface salinity (SSS, in g/kg) from the FORM and SKIN runs in December-January-February (DJF) (15a, 15c) and June-July-August (JJA) (15b, 15d) in the Northern (15a, 15b) and Southern (15a, 15d) Hemispheres.

to the form drag formalism in NEMO-LIM3, the differences in F_w between the two model runs may not alone explain the changes in SSS. The spatial distributions of the differences in F_w between the two runs do not coincide (not shown) with the ones in SSS (Figure 15). The form drag formulation enhances the freshwater input to the ocean surface in the CAA, and the peripheral Arctic Seas but damps this input in the Central Arctic. In the Antarctic, the two simulations exhibit regional differences in the summer mean of F_w. When including form drag, the freshwater input to the ocean surface is higher in the Weddell and Davis Seas (around 90 °E) but is smaller in the other Antarctic regions. These differences disagree with the near-ubiquitous increase in SSS in the Antarctic ice pack and the freshening of the Antarctic MIZ during the austral summer.

Does form drag impact the seasonality of the SSS through changes in ocean surface stresses? Castellani et al. (2018) simulated an increase in the mean Arctic SSS in summer and a fresher Beaufort Gyre when selecting the form drag scheme of Steiner (2001) in their model. These findings agree with the form drag effects on the simulated SSS in the Northern Hemisphere. The differences in the form drag implementation between our study and the one of Castellani et al. (2018) point to an effect of the form drag on the ocean surface stress to explain the changes in Arctic SSS. We find a spatial correspondence between the seasonal differences in ocean surface stress (Figure 13) and the differences in SSS (Figure 15). The fresher Beaufort Gyre simulated when activating the form drag scheme is consistent with the increased ocean surface stress (Roy et al., 2015). The higher summer mean ocean surface stress in the FORM run leads to a more efficient mixing of the water masses and a less stratified ocean surface layer than in the reference SKIN run. Obviously, the underestimation of the prescribed floe lengths in the Arctic likely plays a role in the summer intensification of the ocean surface stress. This issue is probably less important in the Antarctic. The agreement of our results with the ones of Castellani et al. (2018) confirms the importance of form drag for the seasonality of form drag for the SSS under sea ice.

3.3.3. Mixed layer depth

The ocean mixed layer depth (denoted ML hereafter) corresponds to the thickness of the quasi-homogeneous layer in the upper ocean. Ocean surface fluxes of heat, momentum and mass control the seasonal cycle of the ML depth. Sea ice mediates the ocean surface fluxes in the polar regions: the melting and freezing of sea ice act on the upper ocean stratification; the sea ice concentration modulates the heat exchanges between the atmosphere and the ocean; the ice-ocean drag stirs the upper ocean surface. Usually, a property difference or a gradient criterion relative to a reference depth defines the ML depth (Kara et al., 2000). We define the ML depth in NEMO-LIM3 as the depth at which the density is $0.01\,\mathrm{kg/m^3}$ higher than the density at 10 m depth. This definition likely overestimates the simulated ML depth in deep convection regions (Courtois et al., 2017) but is appropriate for polar regions (Peralta-Ferriz and Woodgate, 2015).

The seasonal changes in ML depth are more intense in the open ocean at high latitudes, such as in the Norwegian Sea or the Southern Ocean. The presence of sea ice strongly inhibits these seasonal changes in ML depth. In the FORM run, the Arctic mean ML depth under sea ice is 13 m in summer and 36 m in winter (Figure 16). The simulated ML depth reaches $\sim$70 m during winter in the Central Arctic. These results agree with observed Arctic ML depths over the past decades (Peralta-Ferriz and Woodgate, 2015). In the Antarctic, the mean ML depth under sea ice is 17 m in summer and 83 m in winter in the FORM run. The simulated ML is deeper along the coast of Antarctica during winter (Figure 16d). Pellichero et al. (2017) found using various observations similar spatial distributions of the Antarctic ML depth during the summer and winter months.

The form drag scheme strongly influences the simulation of the ML depth in ice-covered regions, especially in summer (Figure 17). The summer mean ML depths under sea ice are 22 % to 38 % larger in the FORM run with respect to the SKIN run in the Arctic and Antarctic, respectively. The overestimation of the summer neutral drag coefficients likely enhances these modelled differences. Nonetheless, the FORM run exhibits a year-long deep ML in the Central Arctic not featured in the SKIN run. Such a deep ML in the FORM run agrees with the observations of a mean ML depth between 50 and 70 m during winter in the Makarov and Eurasian basin (Peralta-Ferriz and Woodgate, 2015). Moreover, Castellani et al. (2018) reported a seasonal deepening of the Arctic ML when using the form drag scheme of Steiner (2001). The base of the winter ML under the Antarctic sea ice is 10 m shallower in the FORM run than in the reference SKIN run (Figure 17c). The changes in the ML depth along the coastline of Antarctica are evidence of the strong sensitivity of the ML to the form drag formalism.

Hydrographic profiles show a nearly ubiquitous shoaling of the Arctic ML from 1979 to 2012 (Peralta-Ferriz and Woodgate, 2015). According to these authors and Petty et al. (2014), winds affect the ML only in the absence of sea

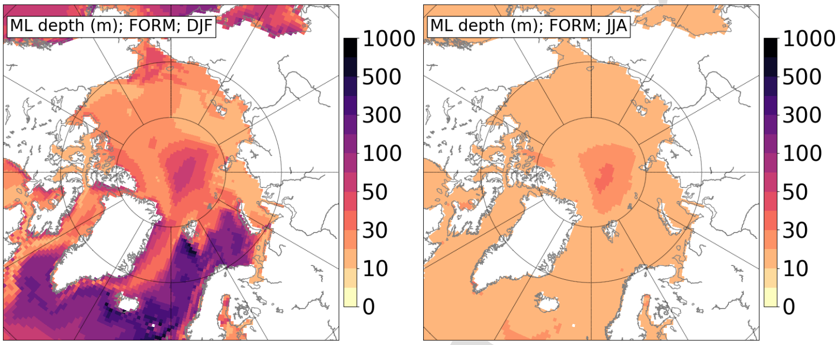

(a) (b)

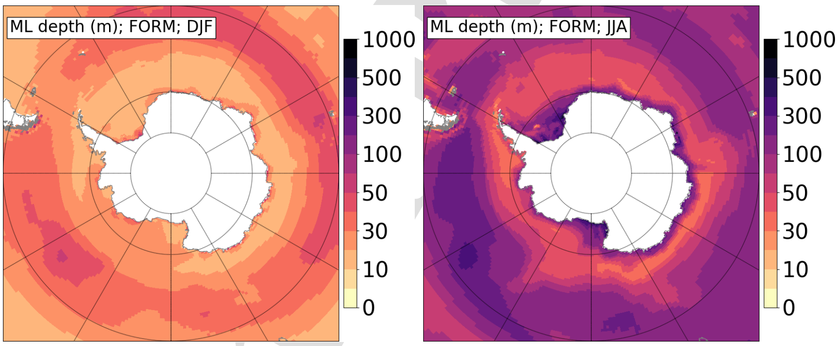

(c) (d)

Figure 16: Seasonal mean (1980–2019) mixed layer depths (m) from the FORM run in December-January-February (DJF) (16a, 16c) and June-July-August (JJA) (16b, 16d) in the Northern (16a, 16b) and Southern (16a, 16d) Hemispheres.

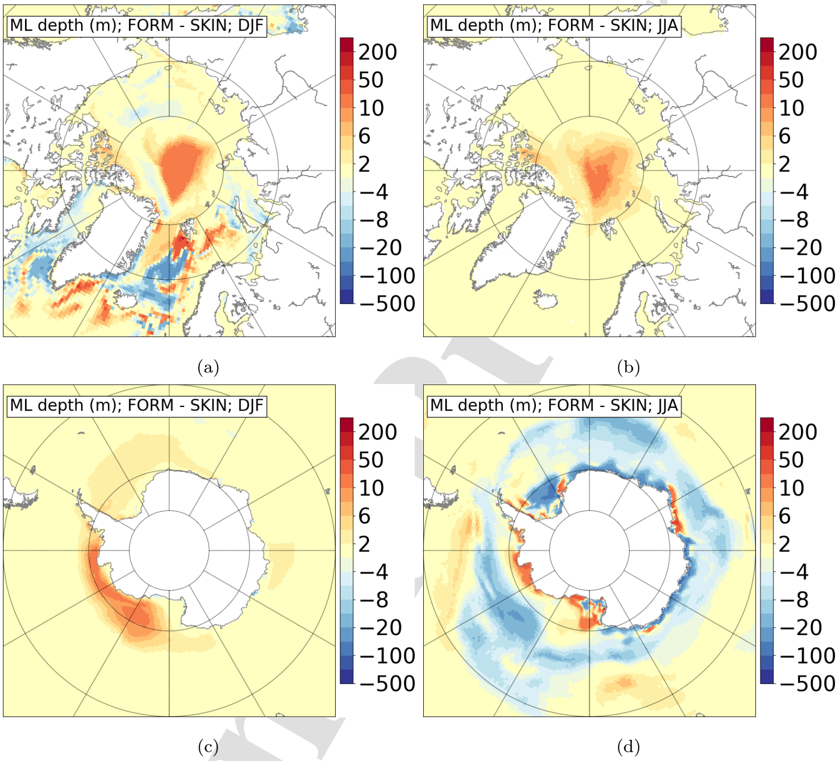

Figure 17: Differences in seasonal mean (1980–2019) mixed layer depth (m) between the FORM and SKIN runs in December-January-February (DJF) (17a, 17c) and June-July-August (JJA) (17b, 17d) in the Northern (17a, 17b) and Southern (17a, 17d) Hemispheres.

ice. NEMO-LIM3 captures the observed shoaling of the ML in the Central Arctic only (Figure 18a). In the model, the Arctic regions experiencing ML deepening correspond to regions undergoing significant negative trends in sea ice concentration. The modelled sea ice losses in the peripheral Arctic Seas allow for a greater action of wind stress over the open water fractions and hence ML deepening.

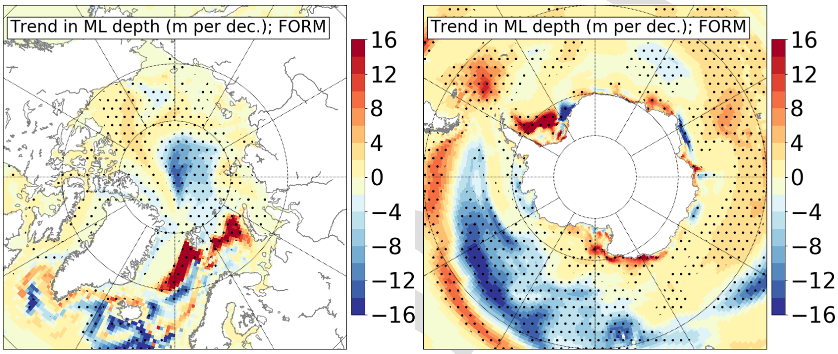

(a) (b)

Figure 18: Trends in the annual mean mixed layer depth (m per decade) over 1980–2019 from the FORM in the Northern (18a) and Southern (18b) Hemispheres. Dots indicate a p-value less than 0.1.

The spatial distribution of the trends in Arctic ML depth is similar in the FORM and SKIN runs. However, the modelled trends differ in magnitude (Figure 19a). In the Central Arctic, the trends in ML depth are approximately -11 m per decade in the FORM run and -4 m per decade in the SKIN run. These modelled trends are close to the observed rate of -10 m to -5 m reported by Peralta-Ferriz and Woodgate (2015). These authors claim that the freshening of the Arctic ML is the principal driver of the ML shoaling in the Arctic. In our model runs, the trends in the annual mean Arctic SSS are nearly equal in the two runs (-0.11 g/kg per decade in the FORM run and -0.10 g/kg per decade in the SKIN run). Consequently, the form drag parameterization does not question the model's ability to represent the freshening of the Arctic Ocean close to the surface. On the other hand, form drag modulates the trends in Arctic ML depth in our model setup.

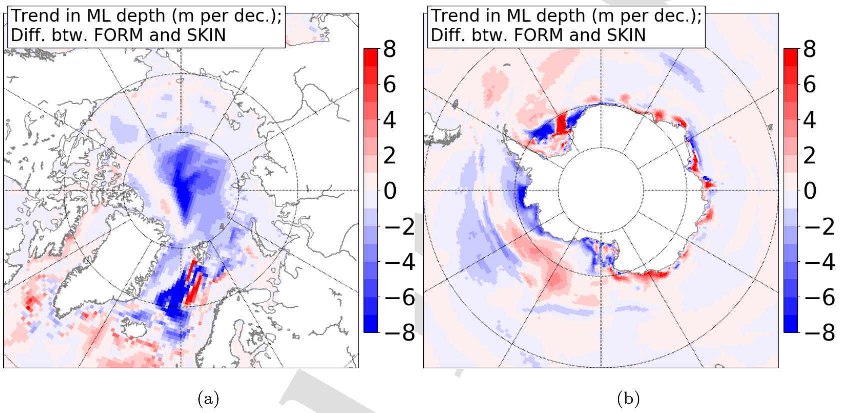

Figure 19: Differences between the trends in the annual mean mixed layer depth (m per decade) over 1980–2019 from the FORM and the SKIN runs in the Northern (19a) and Southern (19b) Hemispheres.

In the Southern Hemisphere, the modelled interdecadal trends in ML depth have almost the same spatial distribution except in the Bellingshausen Sea. The modelled ML in the FORM run shoals in the Weddell and Ross Seas but deepens in the BA Seas (Figure 19b). In the SKIN run, the trend in the mean BA Seas ML depth is not significant. The ML depth trends from the two simulations differ locally by about ± 10 m per decade along the coastline of Antarctica (Figure 19b). These differences drop to levels below

∼2 m in the Antarctic ice pack.

4. Conclusion

In this study, we implemented the form drag formalism of Tsamados et al. (2014) into the fully coupled ocean–sea ice model NEMO-LIM3. Using a global configuration of this model, we performed one simulation accounting for the form drag over sea ice and a second with constant neutral drag coefficients over sea ice. In the second simulation, the drag coefficients over sea ice are set equal to the mean of the variable neutral drag coefficients over sea ice from the first simulation. Using these two simulations, we investigated the effect of the form drag on the sea ice cover and ocean surface properties in both the Arctic and Antarctic over the past four decades.

Past model studies showed the interest in including form drag over sea ice in climate models (Tsamados et al., 2014; Castellani et al., 2018; Chikhar et al., 2019). Martin et al. (2016) and their predecessors (Tsamados et al., 2014) relied on a stand-alone version of CICE. This excludes feedback mechanisms between the ocean and sea ice or the atmosphere. Our configuration of NEMO-LIM3 features a full coupling of ocean and sea ice models forced by an atmospheric reanalysis surface product, as in the model studies of Castellani et al. (2018) and Chikhar et al. (2019). We improve upon the study of Castellani et al. (2018) thanks to our refined ocean vertical grid, the integration of a sea ice strength parameterization and an ITD in the model. Moreover, the form drag formalism of Tsamados et al. (2014) is conceptually different from the scheme of Steiner (2001) used by Castellani et al. (2018). Lastly, our simulations are global, allowing investigation of the form drag effect in the Antarctic and Arctic regions.

The salient points of our study are:

1. The form drag scheme significantly affects the modelled sea ice thickness and volume in NEMO-LIM3. Sea ice is 0.1–0.5 m thinner in the peripheral seas of the Arctic basin and the coastal region of the BA Seas but generally 0.1 m thicker in the Antarctic ice pack with form drag. The impact is small on the simulated sea ice concentration and area, with only very small differences in the peripheral seas of the Arctic basin and the Antarctic MIZ. These differences relate to the ones in sea ice thickness.
2. The form drag formulation weakly impacts the simulated sea ice drift. The relative difference between the two model runs in sea ice drift speed is less than 10 % in the Central Arctic and Antarctic ice pack. Sea ice drift speeds in the CAA are sensibly higher when activating the form drag scheme. The differences in the simulated trend in sea ice drift speed suggest a long-term effect of the form drag on the sea ice drift.
3. The simulated ANDC and ONDC exhibit a spatial and seasonal variability pertinent for sea ice and ocean modelling. The simulated coefficients are maximum in summer and minimum in winter. However, form drag is in all likelihood overestimated in summer because of the prescribed floe length formulation of Lüpkes et al. (2012) (Brenner et al., 2021; Bateson, 2021). The coefficients are high in the CAA, Fram Strait and the western sector of the Antarctic (Weddell, BA and Ross Seas). These coefficients experience a negative trend in the Arctic over 1980-2019. In the Antarctic, the trends in these coefficients are positive in

the Ross and Weddell Seas and negative in the BA Seas. The trends in the neutral drag coefficients are principally driven by the form drag contribution of sails and keels.

4. The formulation of the neutral drag coefficients strongly impacts the ocean surface stress in polar regions. In our model runs, the seasonality of the variable ANDC and ONDC damps (enhances) the ocean surface stress under sea ice in winter (summer). The enhanced summer ocean surface stress simulated with form drag needs to be confirmed with a more realistic floe size formulation. On the other hand, the simulated decrease in deformed ice fractions, the associated decline in form drag and the negative trend in the ocean surface stress in the Arctic regions show some correspondence with the observed decline in Arctic MYI over 1980-2019. This confirms the results of Martin et al. (2016) for the Arctic regions. The regional trends in the Antarctic ocean surface stress differ significantly depending on the inclusion of form drag. The annual mean ocean surface stress increases with time in the Weddell and Ross Seas but decreases in the BA Seas with form drag. The signs of these regional trends agree with the changes in the variable neutral drag coefficients.
5. The simulated SST in polar regions differs in summer and in the MIZ. The summer mean SST in the Arctic MIZ is 0.5 to 1.5 °C higher with form drag, whereas the summer mean SST is approximately $-0.5\,^{\circ}$C smaller in the Antarctic MIZ. Indirect changes in sea ice properties caused by the inclusion of form drag explain nearly all the differences in SST between the two simulations. Form drag increases the SSS by

0.89 g/kg and 0.52 g/kg in summer under the Arctic and Antarctic ice pack, respectively. In the FORM run, the increased summer mean ocean surface stress leads to enhanced vertical mixing, altering the re-stratification of the ocean surface under sea ice during the melt season. The alteration of the Arctic SSS persists in winter, suggesting significant changes in the freshwater content in the Arctic Ocean. The effects of form drag on the Arctic SST and SSS are in line with the results of Castellani et al. (2018), based on a conceptually different form drag scheme.

6. The inclusion of the form drag scheme effectively impacts the simulated ML depth in winter and summer, keeping in mind that the neutral drag coefficients are likely overestimated in summer. These results support the conclusions of Castellani et al. (2018) on the Arctic ML. The summer ML is 22 % and 38 % thicker in the Arctic and Antarctic with form drag, respectively. The form drag induces a year-long deeper ML in the Central Arctic as seen in observations. The differences in the simulated Antarctic ML depth indicate a strong sensitivity of the ML to the inclusion of form drag. The magnitude of the simulated trends in ML depth in both hemispheres is equally sensitive to the form drag.

We have not examined the stability effect in the ocean and atmospheric boundary layers. A stable (unstable) stratification in the boundary layer enhances (damps) turbulent surface fluxes (Birnbaum and Lüpkes, 2002; McPhee, 2012). The addition of stability effects in form drag parameterizations has a non-negligible impact on the transfer coefficients in both the ocean and atmosphere (McPhee, 2012; Lüpkes and Gryanik, 2015). However, these effects are difficult to evaluate in the upper ocean boundary layer (McPhee, 1992; Cole et al., 2017).

The simulated ONDC during summer and in the MIZ suffer from uncertainties associated with the prescribed floe length formulation (Brenner et al., 2021). These uncertainties also influence the simulation of lateral ice melt in the model. The floe size distribution provides a feedback mechanism linking the lateral ice melt and the form drag contribution associated with floe edges. Therefore, we advise future studies to revisit our results with a realistic floe size distribution. More recently, Horvat and Tziperman (2015) and Zhang et al. (2016) introduced prognostic floe size distributions for sea ice models that limit assumptions on the statistics of floes. Either prescribed or prognostic floe size distributions are promising in better representing floe sizes in climate models (Bateson et al., 2022).

The impact of form drag on the ocean surface is significant in our simulations with the following caveat that our study is more a sensitivity study than a modelling study aiming for performance against observations. Furthermore, our conclusions might change in a fully coupled ocean-ice-atmosphere model setup. Recent experiments performed with such model setups show effects on the large-scale oceanic and atmospheric circulations (Ponsoni et al., 2021). Accounting for form drag over sea ice is one step towards a better computation of the turbulent fluxes in polar regions.

5. Acknowledgements

Computational resources have been provided by the supercomputing facilities of the Université catholique de Louvain (CISM/UCLouvain) and the

Consortium des Equipements de Calcul Intensif en Fédération Wallonie Bruxelles (CECI) funded by the F.R.S.-FNRS under convention 2.5020.11. François Massonnet is a F.R.S.-FNRS Research Associate. Michel Tsamados acknowledges support from the ESA "CryoSat + Antarctica Ocean" project (ESA AO/1-9156/17/I-BG). The research leading to these results has received funding from the European Commission's Horizon 2020 APPLICATE (GA 727862) and PRIMAVERA (GA 641727) projects. We also thank the anonymous reviewers for their helpful comments on this manuscript.

References

Andreas, E., Horst, T., Grachev, A., Persson, P.O.G., Fairall, C.W., Guest, P.S., Jordan, R.E., 2010. Parametrizing turbulent exchange over summer sea ice and the marginal ice zone. Quarterly Journal of the Royal Meteorological Society 136, 927–943. URL: https://doi.org/10.1002/qj.618, doi:10/dhtbbm. publisher: Wiley.

Arya, S.P.S., 1973. Contribution of form drag on pressure ridges to the air stress on Arctic ice. Journal of Geophysical Research 78, 7092–7099. URL: https://doi.org/10.1029/jc078i030p07092, doi:10/d62s3k.

Arya, S.P.S., 1975. A drag partition theory for determining the large-scale roughness parameter and wind stress on the Arctic pack ice. Journal of Geophysical Research 80, 3447–3454. URL: https://doi.org/10.1029/jc080i024p03447, doi:10/df5x9x.

Barthélemy, A., Goosse, H., Fichefet, T., Lecomte, O., 2017. On the sensitivity of Antarctic sea ice model biases to atmospheric forcing uncertainties. Climate Dynamics URL: https://doi.org/10.1007/s00382-017-3972-7, doi:10/gdx3cz.

Bateson, A.W., 2021. Fragmentation and melting of the seasonal sea ice cover. Ph.D. Thesis. University of Reading. Department of Meteorology. URL: http://centaur.reading.ac.uk/id/eprint/98821. publisher: University of Reading.

Bateson, A.W., Feltham, D.L., Schröder, D., Wang, Y., Hwang, B., Ridley, J.K., Aksenov, Y., 2022. Sea ice floe size: its impact on pan-Arctic and local ice mass and required model complexity. The Cryosphere 16, 2565–2593. URL: https://tc.copernicus.org/articles/16/2565/2022/, doi:10/gq68qg.

Birnbaum, G., Lüpkes, C., 2002. A new parameterization of surface drag in the marginal sea ice zone. Tellus A: Dynamic Meteorology and Oceanography 54, 107–123. URL: https://doi.org/10.3402/tellusa.v54i1.12121, doi:10/fx5qd9.

Bitz, C.M., Lipscomb, W.H., 1999. An energy-conserving thermodynamic model of sea ice. Journal of Geophysical Research: Oceans 104, 15669–15677. URL: https://doi.org/10.1029/1999jc900100, doi:10/bf83pt.

Brenner, S., Rainville, L., Thomson, J., Cole, S., Lee, C., 2021. Comparing observations and parameterizations of ice-ocean drag through an annual cycle across the Beaufort Sea. Journal of Geophysical Research: Oceans URL: https://doi.org/10.1029/2020jc016977, doi:10/gnpwcj. publisher: American Geophysical Union (AGU).

Castellani, G., Losch, M., Ungermann, M., Gerdes, R., 2018. Sea-ice drag as a function of deformation and ice cover: Effects on simulated sea ice and ocean circulation in the Arctic. Ocean Modelling 128, 48–66. URL: https://doi.org/10.1016/j.ocemod.2018.06.002, doi:10/gfvg8k.

Castellani, G., Lüpkes, C., Hendricks, S., Gerdes, R., 2014. Variability of Arctic sea-ice topography and its impact on the atmospheric surface drag. Journal of Geophysical Research: Oceans 119, 6743–6762. doi:10/gd3w2p.

Cavalieri, D., Parkinson, C. L., Gloersen, P., Zwally, H. J., 1996. Sea Ice Concentrations from Nimbus-7 SMMR and DMSP SSM/I-SSMIS Passive Microwave Data, Version 1. URL: http://nsidc.org/data/NSIDC-0051/versions/1, doi:10.5067/8gq8lzqvl0vl.

Chikhar, K., Lemieux, J.F., Dupont, F., Roy, F., Smith, G.C., Brady, M., Howell, S.E.L., Beaini, R., 2019. Sensitivity of Ice Drift to Form Drag and Ice Strength Parameterization in a Coupled Ice–Ocean Model. Atmosphere-Ocean 57, 329–349. URL: https://doi.org/10.1080/07055900.2019.1694859, doi:10/gqm2v7. publisher: Informa UK Limited.

Cole, S.T., Timmermans, M.L., Toole, J.M., Krishfield, R.A., Thwaites, F.T., 2014. Ekman veering, internal waves, and turbulence observed under Arctic sea ice. Journal of Physical Oceanography 44, 1306–1328. doi:10/f5xsxg.

Cole, S.T., Toole, J.M., Lele, R., Timmermans, M.L., Gallaher, S.G., Stanton, T.P., Shaw, W.J., Hwang, B., Maksym, T., Wilkinson, J.P., Ortiz, M., Graber, H., Rainville, L., Petty, A.A., Farrell, S.L., Richter-Menge, J.A., Haas, C., 2017. Ice and ocean velocity in the Arctic marginal ice zone: Ice roughness and momentum transfer. Elementa: Science of the Anthropocene 5. URL: https://doi.org/10.1525/elementa.241, doi:10/gc6v5b. publisher: University of California Press.

Comiso, J.C., Gersten, R.A., Stock, L.V., Turner, J., Perez, G.J., Cho, K., 2017. Positive Trend in the Antarctic Sea Ice Cover and Associated Changes in Surface Temperature. Journal of Climate 30, 2251 – 2267. URL: https://journals.ametsoc.org/view/journals/clim/30/6/jcli-d-16-0408.1.xml, doi:10/f9zw6x. place: Boston MA, USA Publisher: American Meteorological Society.

Courtois, P., Hu, X., Pennelly, C., Spence, P., Myers, P.G., 2017. Mixed layer depth calculation in deep convection regions in ocean numerical models. Ocean Modelling 120, 60–78. URL: https://doi.org/10.1016/j.ocemod.2017.10.007, doi:10/gcq9rx. publisher: Elsevier BV.

Dewey, S., 2019. Evolving Ice-Ocean Dynamics of the Western Arctic. Ph.D. Thesis. University of Washington.

Docquier, D., Massonnet, F., Barthélemy, A., Tandon, N., Lecomte, O., Fichefet, T., 2017. Relationships between Arctic sea ice drift and strength modelled by NEMO-LIM3.6. Cryosphere 11, 2829–2846. doi:10/gcrm47.

Eicken, H., 2002. Tracer studies of pathways and rates of meltwater transport through Arctic summer sea ice. Journal of Geophysical Research 107, 8046. URL: http://doi.wiley.com/10.1029/2000JC000583, doi:10/csp9sv.

Flocco, D., Feltham, D., Turner, A., 2010. Incorporation of a physically based melt pond scheme into the sea ice component of a climate model. Journal of Geophysical Research 115. URL: https://doi.org/10.1029/2009jc005568, doi:10/b9g48j.

Fogt, R.L., Sleinkofer, A.M., Raphael, M.N., Handcock, M.S., 2022. A regime shift in seasonal total Antarctic sea ice extent in the twentieth century. Nature Climate Change 12, 54–62. URL: https://doi.org/10.1038/s41558-021-01254-9, doi:10/gn78b5.

Garbrecht, T., Lüpkes, C., Hartmann, J., Wolff, M., 2002. Atmospheric drag coefficients over sea ice - Validation of a parameterisation concept. Tellus, Series A: Dynamic Meteorology and Oceanography 54, 205–219. doi:10/bwx2cz.

Griffies, S., Biastoch, A., Böning, C., Bryan, F., Danabasoglu, G., Chassignet, E., England, M., Gerdes, R., Haak, H., Hallberg, R., Hazeleger, W., Jungclaus, J., Large, W., Madec, G., Pirani, A., Samuels, B., Scheinert, M., Gupta, A., Severijns, C., Simmons, H., Treguier, A., Winton, M., Yeager, S., Yin, J., 2009. Coordinated Ocean-ice Reference Experiments (COREs). Ocean Modelling 26, 1–46. URL: https://doi.org/10.1016/j.ocemod.2008.08.007, doi:10/ctqkq5.

Guest, P.S., Davidson, K.L., 1991. The aerodynamic roughness of different types of sea ice. Journal of Geophysical Research 96, 4709. URL: https://doi.org/10.1029/90jc02261, doi:10/d9rhmr. publisher: American Geophysical Union (AGU).

Hanssen-Bauer, I., Gjessing, Y.T., 1988. Observations and model calculations of aerodynamic drag on sea ice in the Fram Strait. Tellus A: Dynamic Meteorology and Oceanography 40, 151–161. URL: https://doi.org/10.3402/tellusa.v40i2.11789, doi:10/fxjnkz.

Haumann, F.A., Gruber, N., Münnich, M., Frenger, I., Kern, S., 2016. Sea-ice transport driving Southern Ocean salinity and its recent trends. Nature 537, 89–92. URL: https://doi.org/10.1038/nature19101, doi:10/f83tv4.

Heorton, H.D.B.S., Tsamados, M., Cole, S.T., Ferreira, A.M.G., Berbellini, A., Fox, M., Armitage, T.W.K., 2019. Retrieving Sea Ice Drag Coefficients and Turning Angles From In Situ and Satellite Observations Using an Inverse Modeling Framework. Journal of Geophysical Research: Oceans 124, 6388–6413. URL: https://doi.org/10.1029/2018jc014881, doi:10/gqm2v5. publisher: American Geophysical Union (AGU).

Holland, M.M., Bailey, D.A., Briegleb, B.P., Light, B., Hunke, E., 2012. Improved sea ice shortwave radiation physics in CCSM4: The impact of melt ponds and aerosols on Arctic sea ice. Journal of Climate 25, 1413–1430. URL: https://doi.org/10.1175/jcli-d-11-00078.1, doi:10/cgzmng.

Holland, P.R., Bruneau, N., Enright, C., Losch, M., Kurtz, N.T., Kwok, R., 2014. Modeled Trends in Antarctic Sea Ice Thickness. Journal of Climate 27, 3784 – 3801. URL: https://journals.ametsoc.org/view/journals/clim/27/10/jcli-d-13-00301.1.xml, doi:10/f536h5. place: Boston MA, USA Publisher: American Meteorological Society.

Horvat, C., Tziperman, E., 2015. A prognostic model of the sea-ice floe size and thickness distribution. The Cryosphere 9, 2119–2134. URL: https://doi.org/10.5194/tc-9-2119-2015, doi:10/gb9p4s.

Høyland, K.V., 2002. Consolidation of first-year sea ice ridges. Journal of Geophysical Research 107. URL: https://doi.org/10.1029/2000jc000526, doi:10/dpqqx8. publisher: American Geophysical Union (AGU).

Hunke, E., Allard, R., Bailey, D.A., Blain, P., Craig, A., Dupont, F., DuVivier, A., Grumbine, R., Hebert, D., Holland, M., Jeffery, N., Jean-Francois Lemieux, Osinski, R., Rasmussen, T., Ribergaard, M., Roberts, A., Turner, M., Winton, M., 2021. CICE-Consortium/Icepack: Icepack 1.2.5. Zenodo. URL: https://zenodo.org/record/4671132, doi:10.5281/ZENODO.4671132.

Hunke, E.C., Dukowicz, J.K., 1997. An Elastic–Viscous–Plastic Model for Sea Ice Dynamics. Journal of Physical Oceanography 27, 1849–1867. URL: https://doi.org/10.1175/1520-0485(1997)027<1849:aevpmf>2.0.co;2, doi:10/cprm6g.

Istomina, L., 2020. Retrieval of Sea Ice Surface Melt Using OLCI Data Onboard Sentinel-3, in: AGU Fall Meeting Abstracts, pp. C017–07.

Kara, A.B., Rochford, P.A., Hurlburt, H.E., 2000. An optimal definition for ocean mixed layer depth. Journal of Geophysical Research: Oceans 105, 16803–16821. URL: https://doi.org/10.1029/2000jc900072, doi:10/fdgcgm. publisher: American Geophysical Union (AGU).

Kim, T.W., Ha, H.K., Wåhlin, A.K., Lee, S.H., Kim, C.S., Lee, J.H., Cho, Y.K., 2017. Is Ekman pumping responsible for the seasonal variation of warm circumpolar deep water in the Amundsen Sea? Continental Shelf Research 132, 38–48. URL: https://doi.org/10.1016/j.csr.2016.09.005, doi:10/f3t36b. publisher: Elsevier BV.

Kobayashi, S., Ota, Y., Harada, Y., Ebita, A., Moriya, M., Onoda, H., Onogi, K., Kamahori, H., Kobayashi, C., Endo, H., Miyaoka, K., Takahashi, K., 2015. The JRA-55 Reanalysis: General Specifications and Basic Characteristics. Journal of the Meteorological Society of Japan. Ser. II 93, 5–48. URL: https://doi.org/10.2151/jmsj.2015-001, doi:10/f65v7p.

Kurtz, N.T., Markus, T., 2012. Satellite observations of Antarctic sea ice thickness and volume. Journal of Geophysical Research: Oceans 117. URL: https://agupubs.onlinelibrary.wiley.com/doi/abs/10.1029/2012JC008141, doi:10/gc4n6f. _eprint: https://agupubs.onlinelibrary.wiley.com/doi/pdf/10.1029/2012JC008141.

Kwok, R., 2011. Observational assessment of Arctic Ocean sea ice motion, export, and thickness in CMIP3 climate simulations. Journal of Geophysical Research: Oceans 116. URL: https://agupubs.onlinelibrary.wiley.com/doi/abs/10.1029/2011JC007004, doi:10/fvs3bf. _eprint: https://agupubs.onlinelibrary.wiley.com/doi/pdf/10.1029/2011JC007004.

Kwok, R., 2018. Arctic sea ice thickness, volume, and multiyear ice coverage: losses and coupled variability (1958–2018). Environmental Research Letters 13, 105005. URL: https://doi.org/10.1088/1748-9326/aae3ec, doi:10/ghnxfc. publisher: IOP Publishing.

Kwok, R., Pang, S.S., Kacimi, S., 2017. Sea ice drift in the Southern Ocean: Regional patterns, variability, and trends. Elementa: Science of the Anthropocene 5, 32. URL: https://doi.org/10.1525/elementa.226, doi:10/gc6v49.

Large, W., Yeager, S., 2004. Diurnal to decadal global forcing for ocean and sea-ice models: The data sets and flux climatologies. University Corporation for Atmospheric Research URL: http://opensky.ucar.edu/islandora/object/technotes:434, doi:10/gf86bh.

Large, W.G., Yeager, S.G., 2008. The global climatology of an interannually varying air–sea flux data set. Climate Dynamics 33, 341–364. URL: https://doi.org/10.1007/s00382-008-0441-3, doi:10/dnz36q.

Leppäranta, M., 1983. A Growth Model for Black Ice, Snow Ice and Snow Thickness in Subarctic Basins. Hydrology Research 14, 59–70. URL: https://doi.org/10.2166/nh.1983.0006, doi:10/gqm2vk. publisher: IWA Publishing.

Leppäranta, M., Lensu, M., Kosloff, P., Veitch, B., 1995. The life story of a first-year sea ice ridge. Cold Regions Science and Technology 23, 279–290. doi:10/dzf299. publisher: Elsevier.

Liao, S., Luo, H., Wang, J., Shi, Q., Zhang, J., Yang, Q., 2022. An evaluation of Antarctic sea-ice thickness from the Global Ice-Ocean Modeling and Assimilation System based on in situ and satellite observations. The Cryosphere 16, 1807–1819. URL: https://doi.org/10.5194/tc-16-1807-2022, doi:10/gp56v8. publisher: Copernicus GmbH.

Lipatov, M.A., Volkov, V.A., May, R.I., 2021. Linear Trends in Sea Ice Drift Fields in the Arctic Ocean. Oceanology 61, 297–304. URL: `https://doi.org/10.1134/S0001437021030073`, doi:`10/gqm2wk`.

Lu, P., Li, Z., Cheng, B., Leppäranta, M., 2011. A parameterization of the ice-ocean drag coefficient. Journal of Geophysical Research 116. URL: `https://doi.org/10.1029/2010jc006878`, doi:`10/b5kgg5`.

Lüpkes, C., Birnbaum, G., 2005. Surface drag in the Arctic marginal sea-ice zone: A comparison of different parameterisation concepts. Boundary-Layer Meteorology 117, 179–211. doi:`10/bdt37v`.

Lüpkes, C., Gryanik, V., 2015. A stability-dependent parametrization of transfer coefficients for momentum and heat over polar sea ice to be used in climate models. Journal of Geophysical Research 120, 552–581. doi:`10/f64dd9`.

Lüpkes, C., Gryanik, V., Hartmann, J., Andreas, E., 2012. A parametrization, based on sea ice morphology, of the neutral atmospheric drag coefficients for weather prediction and climate models. Journal of Geophysical Research: Atmospheres 117, n/a–n/a. URL: `https://doi.org/10.1029/2012jd017630`, doi:`10/gdb8rn`.

Madec, G., Bourdallé-Badie, R., Bouttier, P.A., Bricaud, C., Bruciaferri, D., Calvert, D., Chanut, J., Clementi, E., Coward, A., Delrosso, D., Ethé, C., Flavoni, S., Graham, T., Harle, J., Iovino, D., Lea, D., Lévy, C., Lovato, T., Martin, N., Masson, S., Mocavero, S., Paul, J., Rousset, C., Storkey, D., Storto, A., Vancoppenolle, M., 2017. NEMO ocean engine. Zenodo. URL: https://doi.org/10.5281/zenodo.3248739, doi:10.5281/zenodo.3248739.

Madec, G., Imbard, M., 1996. A global ocean mesh to overcome the North Pole singularity. Climate Dynamics 12, 381–388. URL: https://doi.org/10.1007/bf00211684, doi:10/dq9bnf.

Martin, T., Steele, M., Zhang, J., 2014. Seasonality and long-term trend of Arctic Ocean surface stress in a model. Journal of Geophysical Research: Oceans 119, 1723–1738. URL: https://doi.org/10.1002/2013jc009425, doi:10/gqm2vp. publisher: American Geophysical Union (AGU).

Martin, T., Tsamados, M., Schroeder, D., Feltham, D.L., 2016. The impact of variable sea ice roughness on changes in Arctic Ocean surface stress: A model study. Journal of Geophysical Research: Oceans 121, 1931–1952. URL: https://doi.org/10.1002/2015jc011186, doi:10/gqm2vx. publisher: American Geophysical Union (AGU).

Maslanik, J., Stroeve, J., Fowler, C., Emery, W., 2011. Distribution and trends in Arctic sea ice age through spring 2011. Geophysical Research Letters 38, n/a–n/a. URL: https://doi.org/10.1029/2011gl047735, doi:10/cwqb2h.

Massonnet, F., Barthélemy, A., Worou, K., Fichefet, T., Vancoppenolle, M., Rousset, C., Moreno-Chamarro, E., 2019. On the discretization of the ice thickness distribution in the NEMO3.6-LIM3 global ocean–sea ice model. Geoscientific Model Development 12, 3745–3758. URL: https://

doi.org/10.5194/gmd-12-3745-2019, doi:10/gqm2v8. publisher: Copernicus GmbH.

Massonnet, F., Mathiot, P., Fichefet, T., Goosse, H., König Beatty, C., Vancoppenolle, M., Lavergne, T., 2013. A model reconstruction of the Antarctic sea ice thickness and volume changes over 1980-2008 using data assimilation. Ocean Modelling 64, 67–75. doi:10/f4rjdh.

McPhee, M.G., 1980. An analysis of pack ice drift in summer. Sea ice processes and models , 62–75.

McPhee, M.G., 1992. Turbulent heat flux in the upper ocean under sea ice. Journal of Geophysical Research 97, 5365. URL: https://doi.org/10.1029/92jc00239, doi:10/bhwkr7. publisher: American Geophysical Union (AGU).

McPhee, M.G., 2012. Advances in understanding ice–ocean stress during and since AIDJEX. Cold Regions Science and Technology 76-77, 24–36. URL: https://doi.org/10.1016/j.coldregions.2011.05.001, doi:10/bt4mj9. publisher: Elsevier BV.

Meneghello, G., Doddridge, E., Marshall, J., Scott, J., Campin, J.M., 2020. Exploring the Role of the "Ice–Ocean Governor" and Mesoscale Eddies in the Equilibration of the Beaufort Gyre: Lessons from Observations. Journal of Physical Oceanography 50, 269 – 277. URL: https://journals.ametsoc.org/view/journals/phoc/50/1/jpo-d-18-0223.1.xml, doi:10/gpvqf7. place: Boston MA, USA Publisher: American Meteorological Society.

Meneghello, G., Marshall, J., Campin, J.M., Doddridge, E., Timmermans, M.L., 2018. The Ice-Ocean Governor: Ice-Ocean Stress Feedback Limits Beaufort Gyre Spin-Up. Geophysical Research Letters 45, 11,293–11,299. URL: https://agupubs.onlinelibrary.wiley.com/doi/abs/10.1029/2018GL080171, doi:10/gfdc3c. _eprint: https://agupubs.onlinelibrary.wiley.com/doi/pdf/10.1029/2018GL080171.

Meneghello, G., Marshall, J., Cole, S.T., Timmermans, M.L., 2017. Observational Inferences of Lateral Eddy Diffusivity in the Halocline of the Beaufort Gyre. Geophysical Research Letters 44, 12,331–12,338. URL: https://agupubs.onlinelibrary.wiley.com/doi/abs/10.1002/2017GL075126, doi:10/gcw4pg. _eprint: https://agupubs.onlinelibrary.wiley.com/doi/pdf/10.1002/2017GL075126.

Nihashi, S., Ohshima, K.I., 2015. Circumpolar Mapping of Antarctic Coastal Polynyas and Landfast Sea Ice: Relationship and Variability. Journal of Climate 28, 3650–3670. URL: https://doi.org/10.1175/JCLI-D-14-00369.1, doi:10/f695kp.

Olason, E., Notz, D., 2014. Drivers of variability in Arctic sea-ice drift speed. Journal of Geophysical Research: Oceans 119. doi:10/gd23vq.

Parkinson, C.L., 2019. A 40-y record reveals gradual Antarctic sea ice increases followed by decreases at rates far exceeding the rates seen in the Arctic. Proceedings of the National Academy of Sciences 116, 14414–14423. URL: https://www.pnas.org/doi/abs/10.1073/pnas.1906556116, doi:10/gf56gd. _eprint: https://www.pnas.org/doi/pdf/10.1073/pnas.1906556116.

Pellichero, V., Sallée, J.B., Schmidtko, S., Roquet, F., Charrassin, J.B., 2017. The ocean mixed layer under Southern Ocean sea-ice: Seasonal cycle and forcing. Journal of Geophysical Research: Oceans 122, 1608–1633. URL: https://doi.org/10.1002/2016jc011970, doi:10/f9zsq2. publisher: American Geophysical Union (AGU).

Peralta-Ferriz, C., Woodgate, R.A., 2015. Seasonal and interannual variability of pan-Arctic surface mixed layer properties from 1979 to 2012 from hydrographic data, and the dominance of stratification for multiyear mixed layer depth shoaling. Progress in Oceanography 134, 19–53. URL: https://www.sciencedirect.com/science/article/pii/S0079661114002158, doi:10/gjpjjd.

Peterson, A.K., Fer, I., McPhee, M.G., Randelhoff, A., 2017. Turbulent heat and momentum fluxes in the upper ocean under Arctic sea ice. Journal of Geophysical Research: Oceans 122, 1439–1456. URL: https://agupubs.onlinelibrary.wiley.com/doi/abs/10.1002/2016JC012283, doi:10/f9zprx. _eprint: https://agupubs.onlinelibrary.wiley.com/doi/pdf/10.1002/2016JC012283.

Petty, A., Tsamados, M., Kurtz, N.T., 2017. Atmospheric form drag coefficients over Arctic sea ice using remotely sensed ice topography data, spring 2009-2015. Journal of Geophysical Research: Earth Surface 122, 1472–1490. URL: https://doi.org/10.1002/2017jf004209, doi:10/gcrnhj.

Petty, A.A., Holland, P.R., Feltham, D.L., 2014. Sea ice and the ocean mixed layer over the Antarctic shelf seas. The Cryosphere 8, 761–783. doi:10/f52kxw. publisher: Copernicus GmbH.

Ponsoni, L., Gupta, M., Sterlin, J., Massonnet, F., Fichefet, T., Hinrichs, C., Semmler, T., Arduini, G., Ridley, J., Nummelin, A., Msadek, R., Terray, L., Salas y Melia, D., Svensson, G., Blockley, E., 2021. APPLICATE deliverable 2.5. Final report on model developments and their evaluation in coupled mode. Deliverable D2.5. Zenodo. URL: https://zenodo.org/record/4916934, doi:10.5281/ZENODO.4916934.

Rackow, T., Danilov, S., Goessling, H.F., Hellmer, H.H., Sein, D.V., Semmler, T., Sidorenko, D., Jung, T., 2022. Delayed Antarctic sea-ice decline in high-resolution climate change simulations. Nature Communications 13, 637. URL: https://doi.org/10.1038/s41467-022-28259-y, doi:10/gpsqxc.

Rampal, P., Weiss, J., Marsan, D., 2009. Positive trend in the mean speed and deformation rate of Arctic sea ice, 1979–2007. Journal of Geophysical Research 114. URL: https://doi.org/10.1029/2008jc005066, doi:10/dbx73d. publisher: American Geophysical Union (AGU).

Randelhoff, A., Sundfjord, A., Renner, A.H.H., 2014. Effects of a Shallow Pycnocline and Surface Meltwater on Sea Ice–Ocean Drag and Turbulent Heat Flux. Journal of Physical Oceanography 44, 2176–2190. URL: https://doi.org/10.1175/jpo-d-13-0231.1, doi:10/f6dn79. publisher: American Meteorological Society.

Roach, L.A., Horvat, C., Dean, S.M., Bitz, C.M., 2018. An Emergent Sea Ice Floe Size Distribution in a Global Coupled Ocean-Sea Ice Model. Journal of Geophysical Research: Oceans URL: https://doi.org/10.1029/2017jc013692, doi:10/gd4m4p.

Rousset, C., Vancoppenolle, M., Madec, G., Fichefet, T., Flavoni, S., Barthélemy, A., Benshila, R., Chanut, J., Levy, C., Masson, S., Vivier, F., 2015. The Louvain-La-Neuve sea ice model LIM3.6: global and regional capabilities. Geoscientific Model Development 8, 2991–3005. URL: https://doi.org/10.5194/gmd-8-2991-2015, doi:10/gb9m82.

Roy, F., Chevallier, M., Smith, G.C., Dupont, F., Garric, G., Lemieux, J.F., Lu, Y., Davidson, F., 2015. Arctic sea ice and freshwater sensitivity to the treatment of the atmosphere-ice-ocean surface layer. Journal of Geophysical Research: Oceans 120, 4392–4417. URL: https://agupubs.onlinelibrary.wiley.com/doi/abs/10.1002/2014JC010677, doi:10/gqm2vr. _eprint: https://agupubs.onlinelibrary.wiley.com/doi/pdf/10.1002/2014JC010677.

Schröder, D., 2003. On the parameterization of turbulent surface fluxes over heterogeneous sea ice surfaces. Journal of Geophysical Research 108. URL: https://doi.org/10.1029/2002jc001385, doi:10/dcms2w.

Schweiger, A., Lindsay, R., Zhang, J., Steele, M., Stern, H., Kwok, R., 2011. Uncertainty in modeled Arctic sea ice volume. Journal of Geophysical Research 116. URL: https://doi.org/10.1029/2011jc007084, doi:10/bt9px4.

Serreze, M.C., Meier, W.N., 2018. The Arctic's sea ice cover: trends, variability, predictability, and comparisons to the Antarctic. Annals of the New York Academy of Sciences 1436, 36–53. URL: https://doi.org/10.1111/nyas.13856, doi:10/gdpc4m.

Shaw, W.J., Stanton, T.P., McPhee, M.G., Kikuchi, T., 2008. Estimates of surface roughness length in heterogeneous under-ice boundary layers. Journal of Geophysical Research 113. URL: https://doi.org/10.1029/2007jc004550, doi:10/bqdszp. publisher: American Geophysical Union (AGU).

Shi, Q., Yang, Q., Mu, L., Wang, J., Massonnet, F., Mazloff, M.R., 2021. Evaluation of sea-ice thickness from four reanalyses in the Antarctic Weddell Sea. The Cryosphere 15, 31–47. URL: https://tc.copernicus.org/articles/15/31/2021/, doi:10/gqm2wg.

Shirasawa, K., Ingram, R.G., 1991. Characteristics of the turbulent oceanic boundary layer under sea ice. Part 1: A review of the ice-ocean boundary layer. Journal of Marine Systems 2, 153–160. URL: https://doi.org/10.1016/0924-7963(91)90021-l, doi:10/b3vx69. publisher: Elsevier BV.

Steiner, N., 2001. Introduction of variable drag coefficients into sea-ice models. Annals of Glaciology 33, 181–186. URL: https://doi.org/10.3189/172756401781818149, doi:10/cst5w6. publisher: Cambridge University Press (CUP).

Sterlin, J., Fichefet, T., Massonnet, F., Lecomte, O., Vancoppenolle, M., 2021. Sensitivity of Arctic sea ice to melt pond processes and atmospheric forcing: A model study. Ocean Modelling 167, 101872. URL: https://www.sciencedirect.com/science/article/pii/S1463500321001256, doi:10/gqfhgc.

Stroeve, J., Notz, D., 2018. Changing state of Arctic sea ice across all seasons.

Environmental Research Letters 13, 103001. URL: https://doi.org/10.1088/1748-9326/aade56, doi:10/gfrj9q.

Strub-Klein, L., Sudom, D., 2012. A comprehensive analysis of the morphology of first-year sea ice ridges. Cold Regions Science and Technology 82, 94–109. URL: https://doi.org/10.1016/j.coldregions.2012.05.014, doi:10/f36wn2.

Sumata, H., Gerdes, R., Kauker, F., Karcher, M., 2015. Empirical error functions for monthly mean Arctic sea-ice drift. Journal of Geophysical Research: Oceans 120, 7450–7475. URL: https://doi.org/10.1002/2015jc011151, doi:10/gqm2vv. publisher: American Geophysical Union (AGU).

Sumata, H., Lavergne, T., Girard-Ardhuin, F., Kimura, N., Tschudi, M.A., Kauker, F., Karcher, M., Gerdes, R., 2014. An intercomparison of Arctic ice drift products to deduce uncertainty estimates. Journal of Geophysical Research: Oceans 119, 4887–4921. URL: https://doi.org/10.1002/2013jc009724, doi:10/gqm2vq. publisher: American Geophysical Union (AGU).

Tandon, N.F., Kushner, P.J., Docquier, D., Wettstein, J.J., Li, C., 2018. Reassessing Sea Ice Drift and Its Relationship to Long-Term Arctic Sea Ice Loss in Coupled Climate Models. Journal of Geophysical Research: Oceans 123, 4338–4359. URL: https://doi.org/10.1029/2017jc013697, doi:10/gd35sb.

Thorndike, A.S., Rothrock, D.A., Maykut, G.A., Colony, R., 1975. The thickness distribution of sea ice. Journal of Geophysical Research 80, 4501–4513. URL: https://doi.org/10.1029/jc080i033p04501, doi:10/bsm4ph.

Tin, T., Jeffries, M.O., 2003. Morphology of deformed first-year sea ice features in the Southern Ocean. Cold Regions Science and Technology 36, 141–163. URL: https://doi.org/10.1016/s0165-232x(03)00008-9, doi:10/dpjwf4. publisher: Elsevier BV.

Tsamados, M., Feltham, D., Petty, A., Schroeder, D., Flocco, D., 2015. Processes controlling surface, bottom and lateral melt of Arctic sea ice in a state of the art sea ice model. Philosophical Transactions of the Royal Society A: Mathematical, Physical and Engineering Sciences 373, 20140167. URL: https://doi.org/10.1098/rsta.2014.0167, doi:10/gf45m4.

Tsamados, M., Feltham, D., Schroeder, D., Flocco, D., Farrell, S., Kurtz, N., Laxon, S., Bacon, S., 2014. Impact of Variable Atmospheric and Oceanic Form Drag on Simulations of Arctic Sea Ice. Journal of Physical Oceanography 44, 1329–1353. URL: https://doi.org/10.1175/jpo-d-13-0215.1, doi:10/f5xszr.

Tschudi, M., Meier, W. N., Stewart, J. S., Fowler, C., Maslanik, J., 2019. Polar Pathfinder Daily 25 km EASE-Grid Sea Ice Motion Vectors, Version 4.1. URL: http://nsidc.org/data/nsidc-0116/versions/4, doi:10.5067/INAWUWO7QH7B.

Turner, J., Hosking, J.S., Bracegirdle, T.J., Marshall, G.J., Phillips, T., 2015. Recent changes in Antarctic sea ice. Philosophical Transactions of the Royal Society A: Mathematical, Physical and Engineering Sciences 373, 20140163. doi:10/gqm2vs. publisher: The Royal Society Publishing.

Vancoppenolle, M., Fichefet, T., Goosse, H., Bouillon, S., Madec, G., Morales Maqueda, M.Á., 2009. Simulating the mass balance and salinity of Arctic and Antarctic sea ice. 1. Model description and validation. Ocean Modelling 27, 33–53. URL: https://doi.org/10.1016/j.ocemod.2008.10.005, doi:10/b3j8kb.

Wang, X., Key, J., Kwok, R., Zhang, J., 2016. Comparison of Arctic Sea Ice Thickness from Satellites, Aircraft, and PIOMAS Data. Remote Sensing 8. URL: https://www.mdpi.com/2072-4292/8/9/713, doi:10/gqm2vw.

Zhang, J., 2014. Modeling the Impact of Wind Intensification on Antarctic Sea Ice Volume. Journal of Climate 27, 202 – 214. URL: https://journals.ametsoc.org/view/journals/clim/27/1/jcli-d-12-00139.1.xml, doi:10/f5m88n. place: Boston MA, USA Publisher: American Meteorological Society.

Zhang, J., Stern, H., Hwang, B., Schweiger, A., Steele, M., Stark, M., Graber, H.C., 2016. Modeling the seasonal evolution of the Arctic sea ice floe size distribution. Elementa: Science of the Anthropocene 4, 000126. URL: https://doi.org/10.12952/journal.elementa.000126, doi:10/gfvg8v.

Zu, Y., Lu, P., Leppäranta, M., Cheng, B., Li, Z., 2021. On the Form Drag Coefficient Under Ridged Ice: Laboratory Experiments and Numerical Simulations From Ideal Scaling to Deep Water. Journal of Geophysical Research: Oceans 126, e2020JC016976. URL: https://agupubs.onlinelibrary.wiley.com/doi/abs/10.1029/2020JC016976, doi:https://doi.org/10.1029/2020JC016976.

Jean Sterlin: Conceptualization, Methodology, Software, Validation, Formal analysis, Data Curation, Writing - Original Draft, Writing - Review & Editing, Visualization. Michel Tsamados : Conceptualization, Methodology, Software, Validation, Formal analysis, Writing - Original Draft, Writing - Review. Thierry Fichefet and François Massonnet: Conceptualization, Methodology, Formal analysis, Writing - Original Draft, Writing – Review, Resources, Supervision, Project administration, Funding acquisition. Gaia Barbic: Conceptualization, Methodology, Formal analysis, Writing - Original Draft, Visualization.

Declaration of interests

☐The authors declare that they have no known competing financial interests or personal relationships that could have appeared to influence the work reported in this paper.

☒The authors declare the following financial interests/personal relationships which may be considered as potential competing interests:

Jean Sterlin reports financial support was provided by Horizon 2020. Michel Tsamados reports financial support was provided by European Space Agency. Francois Massonnet reports financial support was provided by National Fund for Scientific Research (FNRS). Jean Sterlin reports equipment, drugs, or supplies was provided by Center for High Performance Computing and Mass Storage (CISM). Jean Sterlin reports equipment, drugs, or supplies was provided by Consortium des Équipements de Calcul Intensif (CÉCI). Jean Sterlin reports a relationship with Horizon 2020 that includes: funding grants.